Chapter 5

Adaptive Quantum Monte Carlo Approach States for High-Dimensional Systems

Eric R. Bittner,[a] Donald J. Kouri,[a] Sean Derrickson,[a,b]
and Jeremy B. Maddox[c]
[a] *University of Houston, Department of Chemistry, Houston, TX 77204-5003, USA*
[b] *Oceaneering International, Inc., 11911 FM 529, Houston, TX 77041, USA*
[c] *Western Kentucky University, Department of Chemistry, 1906 College Heights Blvd., Bowling Green, KY 42101, USA*
bittner@uh.edu

We present an overview of our work in developing hydrodynamic-based methods for studying the structure and quantum dynamics of rare-gas clusters. We use a hydrodynamical approach based on the Bohm description of quantum mechanics (QM) to satisfy an orbital-free density functional-like Euler–Lagrange equation for the ground state of the system. In addition, we use an information theoretical approach to obtain the optimal density function derived from a series of statistical sample points in terms of density approximates. These are then used to calculate an approximation to the quantum force in the hydrodynamic description. We also show how this

---

Applied Bohmian Mechanics: From Nanoscale Systems to Cosmology
Edited by Xavier Oriols and Jordi Mompart

ISBN 978-981-4316-39-2 (Hardcover), 978-981-4364-10-2 (eBook)
www.panstanford.com

approach can be extended to finite temperature and use this to examine the thermodynamic properties of rare-gas clusters with up to 100 atoms.

5.1 Introduction

In many-body systems, quantum mechanical effects become important when the de Broglie wavelength of a given atom becomes comparable to the characteristic interatomic interaction length, σ. If we define a characteristic temperature as $T^* = \epsilon / k_B$ in terms of the potential well depth, ϵ, one arrives at what is termed the de Boer ratio [99].

$$\Lambda = \frac{\lambda(T^*)}{\sigma} = \frac{\hbar}{\sigma\sqrt{m\epsilon}} \tag{5.1}$$

which is a useful quantity in determining whether or not quantum mechanical effects are important in a given physical system. In the strictly classical limit, $\Lambda = 0$, while systems with $\Lambda > 0.3$ should be considered strongly quantum mechanical.

Atomic and molecular clusters provide almost ideal laboratory systems for studying quantum versus classical dynamical and structural effects as a function of the size and scale of a given system. For example, the de Boer ratio for Ar clusters $\Lambda_{Ar} \approx 0.03$. As such, quantum effects in Ar clusters and liquids play an insignificant role, and their properties can be accurately modeled using classical molecular dynamics techniques. However, for lighter atoms such as Ne, where $\Lambda_{Ne} \approx 0.1$, quantum mechanical effects are important, especially at low temperatures. Quantum corrections are important even in equilibrium calculations and finite temperature calculations because the quantum character strongly affects the thermodynamics via changes in the ground state structure due to increasing zero-point energies. For example, quantum corrections have been shown to lower solid-to-liquid transition temperatures by approximately 10%, and the zero-point energy for small clusters can equal up to 35% of the classical binding energy.

In this chapter, we present our development of a Bohmian trajectory-based approach for computing the quantum mechanical structure, energetics, and thermodynamics of multiatom systems. These systems are important test cases for both theoretical and computational studies since they are at the crossing point between mesoscopic and microscopic length scales. Hence, quantum confinement and delocalization effects may yet play an important role in their structure and properties. From a computational point of view, these are particularly challenging systems since they have too many degrees of freedom to be tackled by more standard basis set approaches. Furthermore, many of their interesting quantum properties are only manifest at very low temperature, making them challenging systems for path-integral Monte Carlo-based approaches due to the potentially infinitely long imaginary time integration required to reach $T = 0$.

We shall first review the salient features of the Bohmian approach, focusing upon how one might use it to develop new computational approaches for many-body systems. We then present a variational approach that finds the quantum ground state for N-atom rare clusters using a statistical modeling approach for determining a best estimate of the quantum potential for a multidimensional system. We then extend this approach to finite temperature and present results for systems as large as Ne_{100}. In the last part of the chapter, we present an idea based upon supersymmetric (SUSY) QM that extends our approach to excited states. We conclude with a discussion of the prospects of our methods.

5.2 Mixture Modeling Approach

Perhaps the most fundamental objective in statistical analysis pertains to the development of probabilistic models that can explain and predict the observations of interesting physical processes. The capacity to estimate the effectiveness of a statistical model goes hand in hand with the ability to improve its explanatory and predictive powers. Problems related to this idea are encountered throughout the biological, physical, and social sciences. In some cases, it is possible to construct a model that incorporates prior knowledge and experience in terms of a few (or more often many!) adjustable parameters. The primary goal is then to find a particular set of parameters that best explains the observed data and can predict the likely outcome of new observations. The mathematical formalism that quantifies these notions is provided within the Bayesian construction of statistical analysis [68]. In the Bayesian approach, probabilities are treated subjectively as a degree of belief rather than a frequency of observation. Though this distinction is somewhat controversial, Bayesian statistics are crucially important to probabilistic learning [23], decision-making theory, and statistical inference problems. In the quantum physics literature, Bayesian probabilities have recently been addressed in connection with a diverse range of problems, including many-body potential energy surfaces [70, 71], the control of open quantum systems [103], quantum tomography [27], measurement theory in quantum logic devices [59–61, 98], and quantum Monte Carlo simulations [19, 56].

In this section we develop an approximate methodology for estimating the multidimensional quantum distribution function associated with a statistical ensemble of space-time trajectories. The scheme that we propose is built upon a parameterized Gaussian model for the quantum density. We explore the advantages and limitations of this model and outline an iterative procedure based upon Bayesian probability theory for finding a set of Gaussian parameters that mimics the true density function. This fitted density is then used to compute an approximate quantum force that drives the ensemble of trajectories. We show how this approach can be used to determine the ground state density and ground state energy of a multidimensional quantum mechanical system.

5.2.1 *Motivation for a trajectory-based approach*

According to Newton's second law, the physical motion of a particle is characterized by a space-time path $\vec{r}(t)$ that satisfies the equations of motion:

$$\dot{\vec{r}}(t) = \vec{p}(t)/m \tag{5.2}$$

$$\dot{\vec{p}}(t) = -\vec{\nabla} V(\vec{r}(t)) \tag{5.3}$$

where m is the mass of the particle and $-\vec{\nabla} V(\vec{r})$ is the force associated with an externally applied potential energy field. In principle, the position $\vec{r}$ and momentum $\vec{p}$ of a classical particle can be determined with arbitrary precision, and it is well known that exactly specifying the initial conditions $\vec{r}_0 = \vec{r}(0)$ and $\vec{p}_0 = \vec{p}(0)$ will completely determine the particle's trajectory for all time.

In QM, however, the situation is quite different. The precision with which $\vec{r}$ and $\vec{p}$ can be simultaneously known is limited by Heisenberg's uncertainty principle: $\Delta x \Delta p \geq \hbar/2$. The dynamical properties of a particle are embodied in a complex wave function $\psi(\vec{r}, t)$ that satisfies the time-dependent Schrödinger equation:

$$i\hbar\partial_t\psi(\vec{r}, t) = -\frac{\hbar^2}{2m}\vec{\nabla}^2\psi(\vec{r}, t) + V(\vec{r})\psi(\vec{r}, t) \tag{5.4}$$

Traditionally, the wave function is interpreted as a time-dependent amplitude associated with the instantaneous probability of finding the particle in an infinitesimal volume of space $d^3\vec{r}$ about the point $\vec{r}$. From this point of view, individual physical particles are treated as statistical objects and the notion that particles follow definite paths in space-time is apparently a meaningless concept in QM.

One way to rationalize this disparity among the classical and quantum theories is the Feynman path integral approach to QM [41]. According to Feynman's analysis, a path $\vec{r}(t)$ connecting two points in space-time is associated with a complex phase factor $\phi = \exp(iS_{cl}/\hbar)$ determined by the classical action:

$$S_{cl}[\vec{r}(t)] = \int_0^t ds\, \frac{1}{2}m\dot{\vec{r}}^2 - V(\vec{r}) \tag{5.5}$$

along the path. The probability amplitude with which a particle makes a transition from an initial point $(\vec{r}_0, 0)$ to some final point $(\vec{r}_t, t)$ is expressed as the sum of phase factors over all possible paths connecting the two points. For a quantum mechanical particle, no particular path is preferred; therefore, we must consider an infinite number of paths in order to compute the transition probability. For macroscopic objects, however, the classical action is much larger than $\hbar$, implying that the net contribution of phase in the transition amplitude is due to the path that minimizes the classical action. Hence, the most probable path for a macroscopic object will be a trajectory that also satisfies the classical equations of motion. Feynman's treatment is particularly enlightening because it allows us to discuss both classical and quantum mechanical phenomena on an equal footing, that is, in terms of an ensemble of all possible paths that effectively reduces to the classical trajectory in the limit that $\hbar$ is small.

5.2.1.1 Bohmian interpretation

Another formulation of QM in terms of an ensemble of paths is due to the work of de Broglie [31–33] and Bohm [15–17, 52]. In the de Broglie–Bohm interpretation of QM one assumes that a quantum mechanical system is physically composed of two parts, a wave *and* a point particle. Mathematically, the wave is represented by a wave function $\psi(\vec{r}, t)$ that satisfies Eq. (5.4) and is associated with the probability density $\rho(\vec{r}, t) = |\psi(\vec{r}, t)|^2$ for finding the particle when its exact position is unknown. Regardless of whether or not it can be observed, the particle always follows a precisely defined trajectory. The wave function plays a direct physical role in this by influencing the particle's trajectory through the introduction of a nonlocal "quantum potential" that gives rise to all nonclassical behavior, including zero-point energy, tunneling, and self-interference effects.

While the Bohm interpretation of QM is still a subject of philosophical controversy and stimulating debate, it has also, over the past several years, attracted attention in the chemical physics community as a viable framework for the development of novel trajectory-based computational methodologies.

To see this influence, we begin by writing the wave function in complex polar form:

$$\psi(\vec{r}, t) = \rho(\vec{r}, t)^{1/2} \exp(iS(\vec{r}, t)/\hbar) \tag{5.6}$$

where the density $\rho(\vec{r}, t)$ and phase $S(\vec{r}, t)$ (quantum action) are real functions dependent upon space and time. The particle is assumed to follow a definite trajectory $\vec{r}(t)$ along which its velocity:

$$\begin{aligned}\dot{\vec{r}} &= \vec{v}(\vec{r}(t), t)\\ &= \vec{\nabla} S(\vec{r}(t), t)/m\end{aligned} \tag{5.7}$$

is determined by the phase amplitude of the wave function. For notational convenience we will drop the explicit dependence on $\vec{r}$ and t. Substituting Eqs. (5.6) and (5.7) into Schrödinger's equation and equating the real and imaginary components yield a pair of coupled partial differential equations:

$$\partial_t \rho = -\vec{\nabla} \cdot (\rho\, \vec{v}) \tag{5.8}$$

$$\partial_t S = -(Q + V) - \frac{1}{2} m\vec{v}^2 \tag{5.9}$$

which are easily identified as the continuity equation and a generalized Hamilton–Jacobi equation, respectively. The quantum potential term $Q = Q(\vec{r}, t)$, given by:

$$Q = -\frac{\hbar^2}{4m}\left(\frac{\vec{\nabla}^2\rho}{\rho} - \frac{1}{2}\left(\frac{\vec{\nabla}\rho}{\rho}\right)^2\right) \tag{5.10}$$

distinguishes Eq. (5.9) from a purely classical equation and encapsulates the nonlocal influence of ψ on the trajectory of the particle. The quantum potential is often interpreted as an internal energy or "shape" energy associated with the curvature of the quantum density. We can explicitly include Q into the equations of motion for the particle by introducing a material time derivative:

$$d_t f = \partial_t f + \vec{v} \cdot \vec{\nabla} f \tag{5.11}$$

such that the field equations of motion for ρ and S are given by:

$$d_t\rho = -\rho\, \vec{\nabla} \cdot \vec{v} \tag{5.12}$$

$$d_t S = \frac{1}{2}m\vec{v}^2 - (Q + V) \tag{5.13}$$

where the notation d_t signifies the time rate of change in the inertial reference frame of a particle moving along the trajectory $\vec{r}(t)$ with velocity $\vec{v}(\vec{r}(t), t)$. It is evident from the right-hand side of Eq. (5.13) that $d_t S$ represents a generalized Lagrangian $\mathcal{L}(\vec{r}(t), t)$ for the quantum mechanical system. Taking $\vec{\nabla}\mathcal{L}$, we have the relations:

$$\dot{\vec{v}} = -\vec{\nabla}(Q + V)/m \tag{5.14}$$

$$\dot{\vec{r}} = \vec{v} = \vec{\nabla}S/m \tag{5.15}$$

which appear to be a quantum mechanical analogue of Newton's equations that bears a quantum force term $F_Q = -\vec{\nabla}Q$ supplementing the the classical force. We make a special note here to emphasize that the fields ρ, S, $\vec{v}$, and all their derivatives in Eqs. (5.12)–(5.15) are implicitly evaluated along the path $\vec{r} = \vec{r}(t)$, and this path is the trajectory of a physically real point particle, at least within the Bohmian paradigm.

5.2.1.2 Quantum hydrodynamic trajectories

It is fairly obvious from Eqs. (5.12)–(5.15) that if the wave function for a system were known, one would simply need to choose an initial position vector $\vec{r}(0)$ to completely specify the state of the system for all time. While this feature of the Bohmian picture is indeed a useful interpretive tool, we are still faced with the often formidable task of solving the time-dependent Schrödinger equation.

To remedy this situation, we begin by formally introducing an ensemble of quantum trajectories:

$$\mathcal{R}(t) = \{\vec{r}_1(t), \ldots, \vec{r}_n(t)\} \tag{5.16}$$

which are distinguished from one another by their initial positions at time $t = 0$. Just as one can construct a conceptual ensemble of fictitious fluid particles to represent a classical fluid, we have established an analogous ensemble of probability fluid elements to sustain the quantum density, phase, and velocity field. The theoretical groundwork for the evolution of these "particles" has already been laid out. One notable exception is that Eqs. (5.12) and (5.13) are now to be defined over a whole ensemble of quantum trajectories that simultaneously satisfy the set of differential equations given by:

$$\dot{\vec{v}}_i = \vec{\nabla}\mathcal{L}(\vec{r}_i(t), t) \tag{5.17}$$

$$\dot{\vec{r}}_i = \vec{v}_i \tag{5.18}$$

Given an initial wave function $\psi(\vec{r}_i(0), 0)$ defined over the ensemble of points $\mathcal{R}(0)$, we can simultaneously solve Eqs. (5.12) and (5.13) to reconstruct the wave function at a later time t according to the relation:

$$\psi(\vec{r}_i(t), t) = \psi(\vec{r}_i(0), 0) \exp\left(-\frac{1}{2}\int_0^t \vec{\nabla}\cdot\vec{v}(\vec{r}_i(s), s)\, ds\right) \times \exp\left(\frac{i}{\hbar}\int_0^t \mathcal{L}(\vec{r}_i(s), s)\, ds\right) \tag{5.19}$$

where the wave function is represented point-wise along the ensemble of paths $\mathcal{R}(t)$. We emphasize that there is no approximation in Eq. (5.19), and it is a formal solution to the Schrödinger equation evaluated explicitly over a set of hydrodynamic-like quantum trajectories.

A few comments on the behavior of quantum trajectories are in order. First, the single-valuedness of $\psi(\vec{r}, t)$ requires that quantum trajectories must not intersect one another. If two trajectories were to cross, it would imply that the wave function has two distinct values of phase at the same point in space-time. Similarly, trajectories are not allowed to cross through nodal regions of the wave function where the phase is discontinuous and the probability of finding a particle is zero. This restriction is strictly upheld by the influence of the quantum force, which is very intense around nodal surfaces. Moreover, if the ensemble of trajectories are initially distributed according to the probability density $\rho(\vec{r}, 0)$, then the ensemble will be representative of $\rho(\vec{r}, t)$ for all time. This is simply a consequence of the statistical assumption on $\psi(\vec{r}, t)$ and is consistent with the continuity of quantum probability density. Finally, in the limit that $\hbar \rightarrow 0$, the ensemble equations of motion decouple, and the trajectories will evolve independently of one another according to Newton's equations.

In essence, the Bohm picture depicts a quantum mechanical system in terms of an ensemble of correlated particle trajectories. Though the true particle follows a unique trajectory, it is inextricably coupled to an ensemble of alternate paths by the influence of the wave function acting through a quantum force.

5.2.1.3 Computational considerations

Numerical solutions of the time-dependent Schrödinger equation are traditionally obtained by calculating the short-time quantum propagator using fast Fourier transforms [69], finite basis sets, or discrete variable representations [73]. Typically, the computational overhead associated with these techniques scales exponentially with the dimensionality of the physical problem. Trajectory-based methodologies, on the other hand, offer tremendous numerical scaling advantages, especially for high-dimensional systems where traditional techniques are not feasible. In particular, the Bohm interpretation of QM has inspired a growing number of theoretical and computational studies involving a wide range of problems such as reactive scattering dynamics [94, 106], tunneling systems [11, 12, 77, 91], mixed quantum/classical simulations [46–48, 90], electronic transitions [20, 107, 108], photodissociation [38, 53, 85, 102], mixed quantum states [21, 22], and quantum dissipation [80, 81, 109].

The quantum trajectory method (QTM), developed by Wyatt and coworkers [77, 106], incorporates the ideas of computational fluid dynamics to solve the hydrodynamic field equations over a discrete ensemble of quantum fluid elements. Using finite element methods, the fluid particles are arranged into small neighborhoods over which a moving weighted least squares (MWLS) fitting procedure [75] is used to locally expand the hydrodynamic fields ρ (more typically $\log \rho$), S, and $\vec{v}$ in a simple polynomial basis. Once the fields and their derivatives are known, the integrals in Eq. (5.19) along with solutions to Eqs. (5.17)–(5.18) are evaluated over a short time step. While this strategy scales almost linearly with the number of trajectories, its versatility in practice is hindered by the fact that the ensemble of particles generally tends to become extremely disorganized for anharmonic systems making it difficult, if not impossible, to fit the quantum hydrodynamic fields. This becomes especially apparent around the nodes of the wave function, where the fitting errors will oftentimes cause the quantum trajectories to cross one another, leading to spurious numerical results. Very recently [54, 100], new methods in adaptive grids have been developed to formulate a reconstruction of the wave function over an ensemble of generalized hydrodynamic trajectories that avoids the problem with quantum nodes and provides a much more stable framework for solving the hydrodynamic equations of motion.

Another application of the Bohmian apprioach includes the development of semiclassical approximation strategies for including quantum effects into otherwise classical calculations. Garashchuk and Rassolov [42, 43] have recently presented a semiclassical methodology based upon Bohm trajectories that is formally insensitive to trajectory crossings and also avoids explicitly solving the continuity equation. In this approximate methodology, the quantum density is convoluted with a minimum uncertainty Gaussian wave packet and expanded in a linear combination of Gaussian functions:

$$\rho(x) \approx f(x) = \sum_n c_n^2 \exp(-a_n^2(x - X_n)) \tag{5.20}$$

The Gaussian parameters $s = \{c_n, X_n, a_n\}$ in Eq. (5.20) are determined by minimizing the functional:

$$F = \int (\rho(x) - f(x))^2 dx \tag{5.21}$$

using an iterative procedure that explicitly involves solving the set of equations $\partial F/\partial s_k = 0$. The parameterized density leads to an approximate quantum potential (AQP) that is used to propagate an ensemble of trajectories. Garashchuk and Rassolov have presented results for Eckart barrier tunneling that improve upon the Herman–Kluck semiclassical IVR method and are shown to agree quite well with exact quantum mechanical results.

5.2.2 *Density estimation*

5.2.2.1 The mixture model

Suppose that $\mathcal{R} = \{\vec{r}_1, \ldots, \vec{r}_N\}$ is an ensemble of Bohm fluid elements that statistically represents a multidimensional quantum probability density. Such a distribution of data points can be generated from a Metropolis sampling procedure or perhaps from the output of a quantum Monte Carlo simulation [28, 50]. In order to propagate these particles in time, we must evaluate ρ and its derivatives for every member in the ensemble. Instead of solving the hydrodynamic field equations explicitly, we intend to extract this information directly from the ensemble of trajectories.

We assume that the quantum density can be represented by a mixture model [45, 86] determined by summing a finite number, M, of Gaussian components or "clusters." The mixture model decomposition is expressed as a sum of joint probabilities:

$$\rho(\vec{r}) = \sum_{m}^{M} p(\vec{r}, c_m) \tag{5.22}$$

where $p(\vec{r}, c_m)$ is the probability that a randomly chosen member of $\mathcal{R}$ has the configuration $\vec{r}$ and is a variant of the mth Gaussian cluster designated by c_m. Each Gaussian cluster is parameterized by a weight $p(c_m)$, a mean position vector $\vec{\mu}_m$, and a vector of variances $\vec{\sigma}_m^2$. We can also replace the variance vector with a full covariance matrix C_m, if necessary.

By definition [44], each joint probability in Eq. (5.22) is related to a pair of conditional probabilities according to the relation:

$$p(\vec{r}, c_m) = p(c_m)\,p(\vec{r}|c_m) = \rho(\vec{r})\,p(c_m|\vec{r}) \tag{5.23}$$

where the forward conditional probability $p(\vec{r}|c_m)$ refers to the probability that a randomly chosen variant of c_m has the configuration $\vec{r}$. Conversely, the posterior probability $p(c_m|\vec{r})$ refers to the probability that the configuration point $\vec{r}$ is a variant of the cluster c_m. In probability theory the factors $\rho(\vec{r})$ and $p(c_m)$ are marginal probabilities; however, we shall simply refer to them as the quantum density and weight of the mth Gaussian cluster, respectively. The expansion weights are strictly positive semidefinite and sum to unity. Substituting the first equality of Eq. (5.23) into Eq. (5.22), we have:

$$\rho(\vec{r}) = \sum_{m}^{M} p(c_m) p(\vec{r}|c_m) \tag{5.24}$$

where we can specify the form of $p(\vec{r}|c_m)$ to reflect our belief that $\rho(\vec{r})$ is a mixture of Gaussian components. We explore this approximation with two different Gaussian cluster models.

The first model assumes that each cluster is completely separable and takes the form of a product over the N_d-dimensional configuration space:

$$p(\vec{r}|c_m) = \prod_{d}^{N_d} \sqrt{\frac{1}{2\pi\sigma_{m,d}^2}} e^{-(\vec{r}_d-\mu_{m,d})^2/(2\sigma_{m,d}^2)} \tag{5.25}$$

The second model explicitly takes into account nonseparable correlations in configuration space and incorporates the full covariance matrix:

$$p(\vec{r}|c_m) = \sqrt{\frac{||\mathrm{C}_m^{-1}||}{(2\pi)^{N_d}}} e^{-(\vec{r}-\vec{\mu}_m)^T.\mathrm{C}_m^{-1}.(\vec{r}-\vec{\mu}_m)/2} \tag{5.26}$$

In comparison with the separable case, the fully covariant model can represent a more complicated density structures with fewer clusters; however, this is at the cost of greater computational expense. For low-dimensional systems it is advantageous to use the fully covariant model, but in high dimensions it is much more efficient to use a larger number of separable clusters. The principle at work here is related to the idea of collective correspondence discussed by Heller [51] regarding the cooperative effort of overlapping Gaussian wave packets to describe position-momentum correlations in phase space. It is also feasible to construct a mixture model that incorporates any combination of covariant and separable degrees of freedom, especially if there is reason to do so based on the symmetry of the physical problem.

5.2.2.2 Expectation maximization

Now that we have established a model to work with, the trick is to determine the Gaussian parameters $p(c_m)$, $\vec{\mu}_m$, and C_m (or σ_m). The mean position vector and covariance matrix of the clusters are defined by the moments of the forward conditional probabilities:

$$\vec{\mu}_m = \int \vec{r}\; p(\vec{r}|c_m)\, d\vec{r}, \tag{5.27}$$

$$\mathrm{C}_m = \int (\vec{r} - \vec{\mu}_m)^T (\vec{r} - \vec{\mu}_m)\; p(\vec{r}|c_m)\, d\vec{r} \tag{5.28}$$

For the separable case, the variances are given by the diagonal elements $\sigma_{m,i}^2 = (\mathrm{C}_m)_{ii}$. Rearranging Eq. (5.23) and substituting into Eqs. (5.27)–(5.28), we can write these parameters as:

$$\vec{\mu}_m = \int \vec{r}\; \frac{\rho(\vec{r})\, p(c_m|\vec{r})}{p(c_m)}\, d\vec{r} \tag{5.29}$$

$$\mathrm{C}_m = \int (\vec{r} - \vec{\mu}_m)^T (\vec{r} - \vec{\mu}_m) \frac{\rho(\vec{r})\, p(c_m|\vec{r})}{p(c_m)}\, d\vec{r} \tag{5.30}$$

which are easily approximated by a pair of Monte Carlo sums over the ensemble of Bohmian particles:

$$\vec{\mu}_m \approx \frac{1}{N p(c_m)} \sum_n^N \vec{r}_n\, p(c_m|\vec{r}_n) \tag{5.31}$$

$$\mathrm{C}_m \approx \frac{1}{N p(c_m)} \sum_n^N (\vec{r}_n - \vec{\mu}_m)^T (\vec{r}_n - \vec{\mu}_m)\, p(c_m|\vec{r}_n) \tag{5.32}$$

A similar expression for the expansion weights in terms of a sum over $\mathcal{R}$ is given by:

$$p(c_m) \approx \frac{1}{N} \sum_n^N p(c_m|\vec{r}_n) \tag{5.33}$$

The posterior terms $p(c_m|\vec{r}_n)$ for each data point in Eqs. (5.31)–(5.33) are evaluated directly from the forward probabilities according to Bayes's formula:

$$p(c_m|\vec{r}_n) = \frac{p(c_m)\,p(\vec{r}_n|c_m)}{\sum_m p(c_m)\,p(\vec{r}_n|c_m)} \tag{5.34}$$

In some sense, the ensemble of particles can be viewed as a data set that catalogs the results of many successive measurements on an ensemble of identically prepared quantum systems. Each member of the ensemble wields an equal amount of information describing the underlying probability distribution. The key to understanding how this information is distributed among the Gaussian clusters is contained within Bayes's formula. From a Bayesian viewpoint the numerator in Eq. (5.34) essentially boils down to a measure of how well the cluster c_m describes the fluid element with configuration $\vec{r}_n$. The sum in the denominator is a measure of how well the particle at $\vec{r}_n$ is described by all of the clusters. The ratio of the two quantities then determines the fraction of explanatory information that the particle gives to the *m*th cluster. Hence, the cluster that best describes $\vec{r}_n$ will have the largest posterior probability for that point.

The circular structure in Eqs. (5.22)–(5.34) provides the framework for an iterative procedure known as the expectation maximization (EM) algorithm [35, 45, 86] that seeks to find a set of parameters that gives the best estimate for the density of $\mathcal{R}$. Computing the forward and posterior probabilities determines how well an arbitrarily parametrized mixture model is *expected* to represent the ensemble. Evaluating the sums in Eqs. (5.31)–(5.33) gives rise to a new set of parameters that is said to *maximize* the log-likelihood:

$$L = \log \prod_n \rho(\vec{r}_n) \tag{5.35}$$

of the distribution. A likelihood is a probability measure referring to the outcome of an event that is already known to have occurred. The log-likelihood of the distribution is a measure of how well the overall density model describes the entire collection of data points. The EM algorithm works very much like the variational principle, in that, there is a likelihood equation defined over parameter space:

$$\vec{\nabla}_{c_m} L = 0 \tag{5.36}$$

such that L is a maximum for models that are effective in describing the ensemble's distribution. Furthermore, it can be shown that the update rules in Eqs. (5.31)–(5.33) move the clusters through parameter space in the direction along $\vec{\nabla}_{c_m} L$, that is, in the direction that improves the density estimate. The cycle of estimating the expected distribution function, and maximizing the log-likelihood is repeated iteratively until a satisfactory estimate of the density is achieved.

It is important to realize that finding the maximum likelihood estimate of a distribution is not always a well-defined problem. In fact, there are generally multiple roots to the likelihood equation, and it is not necessarily guaranteed that there is a global maximum. While this is an important problem, our main concern here is simply to find an *acceptable* set of parameters that approximately represents the quantum density. However, one problem that we will need to address concerns the number, M, of Gaussian clusters used in the density estimate. For a Gaussian wave packet evolving in a parabolic potential field the answer is simple, but in general we will never really know how many clusters to use. When a wave packet bifurcates at a potential barrier, it will often develop complicated oscillations and nodal structures that are impossible to capture with Gaussians. Though there are statistical methods for "guessing" the number of components in a statistical data set, we do not incorporate them here. Instead, we simply try to use a minimum number of Gaussian clusters that gives reasonable results.

The overall scheme of the mixture model approximation and EM algorithm is as follows: First we generate the ensemble of probability fluid elements, usually a Gaussian density packet, via some appropriate sampling technique. The EM algorithm is initialized by choosing a set of parameters for a preset number of Gaussian clusters. Typically the initial clusters are given a uniform weight $p(c_m) = 1/M$. The mean position vectors are randomly selected from the domain of the ensemble. The initial variances are chosen to be large enough to encompass the entire ensemble, and the cross terms $(\mathrm{C}_m)_{i,j}$ are zero. We cycle through the EM routine until the parameters converge to an acceptable density estimate. Convergence can be evaluated in a number of ways by monitoring the cluster parameters, the conditional probabilities, the log-likelihood, or any combination thereof.

5.2.3 *Computational results*

5.2.3.1 Bivariate distribution with multiple nonseparable Gaussian components

To illustrate some of the points in the previous section, we demonstrate the convergence of the EM algorithm using a known probability distribution function. In Fig. 5.1 we have plotted the

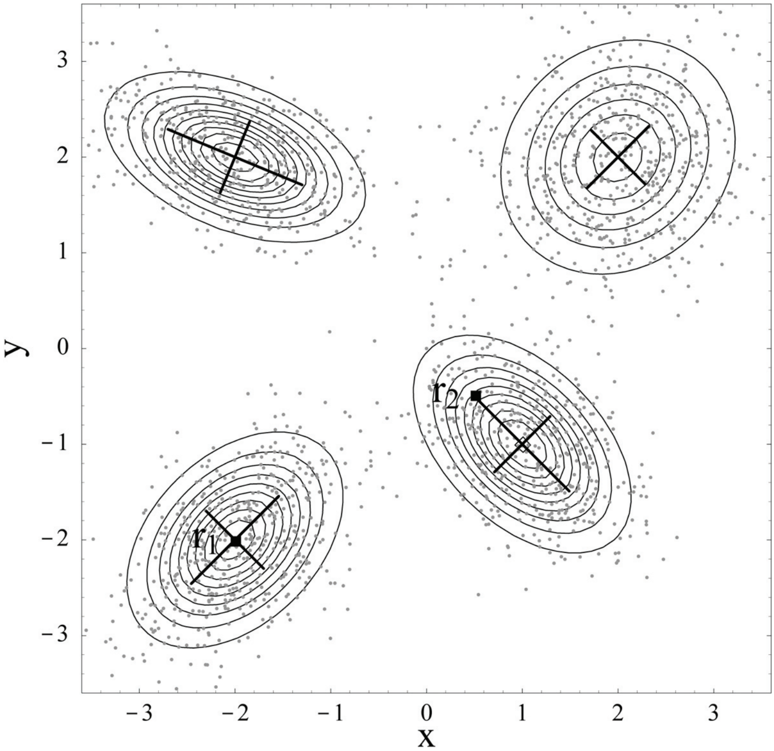

Figure 5.1. The contours reflect a multivariate probability distribution comprised of four Gaussian components with nonzero xy covariances. The solid black lines represent the half-widths of the Gaussian components. The ensemble of gray points are generated from the exact probability distribution function via a Metropolis sampling procedure and are taken as the input data for the EM algorithm. The black squares labeled r_1 and r_2 are tagged data points discussed later in Figs. 5.4 and 5.5. Reprinted with permission from Ref. [82]. Copyright 2003 American Institute of Physics.

contours of a bivariate probability distribution function $\rho(x, y)$ consisting of four equally weighted nonseparable Gaussian components. The solid lines reflect the half-width contours of each component and their orientation with respect to the x and y axes. The gray points correspond to an ensemble $\mathcal{R}$ of 2000 variants of $\rho(x, y)$, which were randomly generated using a Metropolis sampling algorithm. Two of these data points, labeled $\vec{r}_1$ and $\vec{r}_2$, have been tagged for later discussion.

In Fig. 5.2 we show the evolution of 16 separable Gaussian clusters over the course of the EM fitting algorithm. The contour plots indicate the relative intensity of the fitted density at various stages of the EM fit. The black dots and ovals correspond to the μ_m- and σ_m-contours for the individual Gaussian clusters. The initial random guess for the clusters is not illustrated. After 1 EM cycle, the clusters tend to aggregate near the mean of $\mathcal{R}$, and the estimated density does not reflect any details of the exact distribution. After about 10 EM cycles, the clusters begin sorting out the structure of the density. By 100 EM cycles, the clusters have found all four Gaussian components of the distribution and are struggling to recover the proper covariance in each component. The separable clusters are hindered in this because they have no freedom to rotate in the xy plane and must work collectively to capture the xy correlations. At 400 cycles we can see that the separable clusters have performed fairly well in finding the positions and relative orientations of the density components; however, the estimated density is somewhat distorted from the true distribution. The density estimate can be improved by including more sampling points and more clusters, but this also increases the computational demand.

Figure 5.3 illustrates the performance of the fully covariant model using four nonseparable clusters to describe the same data set. As expected, the fully covariant model performs much better than the separable case because the exact probability distribution is rigorously a mixture of four equally weighted nonseparable Gaussian components. After 1 EM cycle, the nonseparable clusters also collect near the mean of $\mathcal{R}$; however, they immediately develop nonzero off-diagonal covariances. Between 10–20 EM cycles, the clusters locate the individual density components. By 50 cycles, the

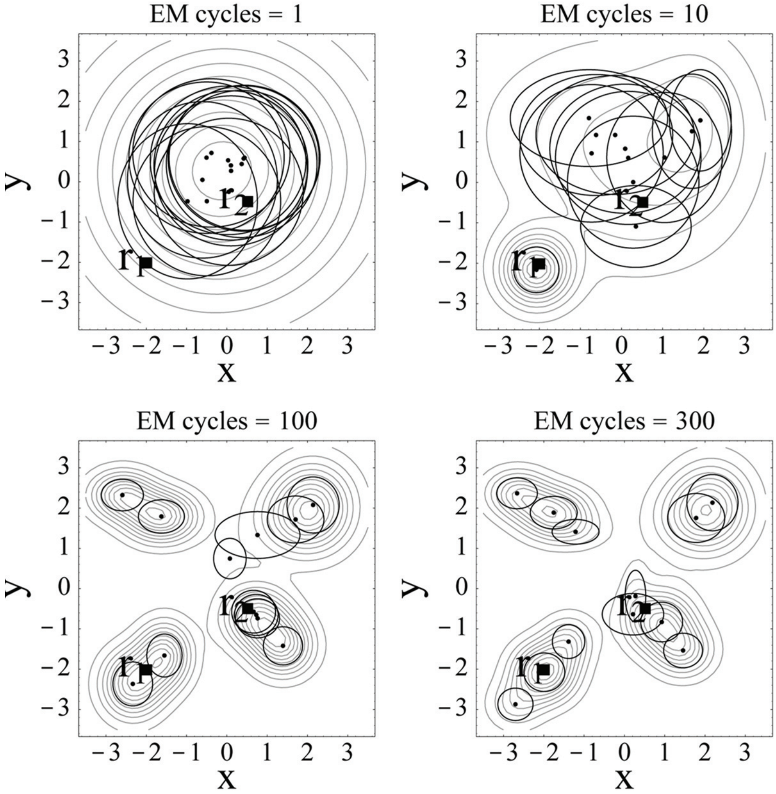

Figure 5.2. This figure illustrates the EM algorithm for the data pictured in Fig. 5.1 using 16 separable Gaussian clusters. The contours reflect the approximated probability density during the course of the EM-fitting routine. The black dots correspond to the average position of the Gaussian cluster, and the solid black ellipses represents the Gaussian half-width contours. Reprinted with permission from Ref. [82]. Copyright 2003 American Institute of Physics.

clusters have established a stable configuration, which very closely mimics the true probability distribution.

Essentially, the EM algorithm performs a parallel search over the Gaussian parameter space and looks for regions where the clusters will be most effective in describing the data points. To help quantify the collective effort of the clusters, we examine the forward and posterior probabilities at the tagged data points $\vec{r}_1$ and

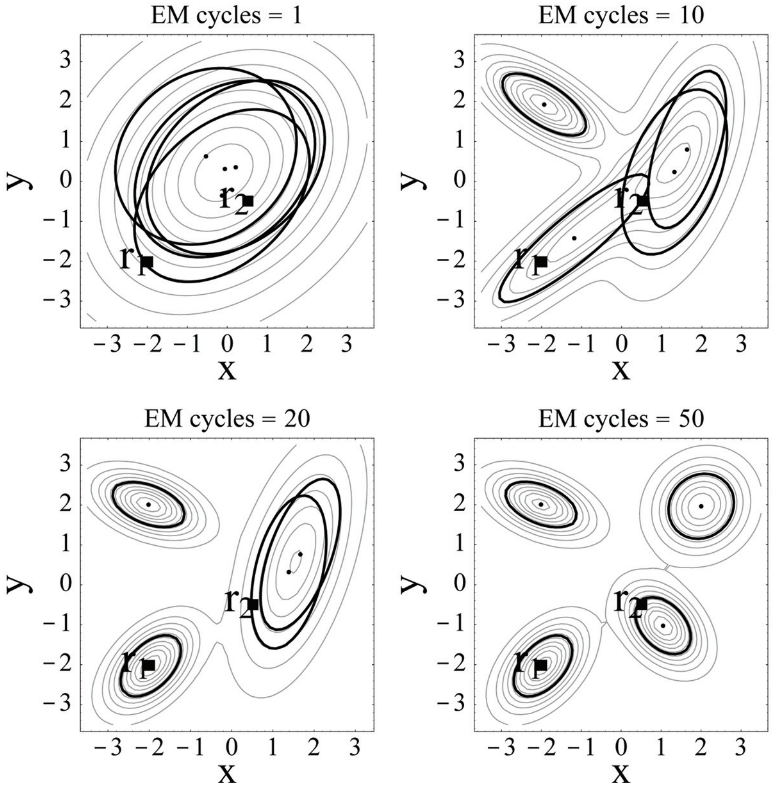

Figure 5.3. This figure illustrates the EM algorithm for the data pictured in Fig. 5.1 using four nonseparable Gaussian clusters. Compared with the separable case, the fully covariant model gives much more accurate results with less clusters and fewer EM cycles. Reprinted with permission from Ref. [82]. Copyright 2003 American Institute of Physics.

$\vec{r}_2$. First, notice in Fig. 5.2 that there are never more than one or two Gaussian clusters centered near the point $\vec{r}_1$. Fig. 5.4a,b shows how the $p(\vec{r}_1|c_m)$'s and $p(c_m|\vec{r}_1)$'s evolve for the separable cluster model. Both plots indicate that for the first 75 EM cycles, there is really only one cluster that dominates the density estimate at $\vec{r}_1$. The posteriors are particularly interesting because they reflect the fraction of explanatory power a data point gives to each of the cluster. The curve crossing at roughly 105 EM cycles reflects that the originally dominant cluster is eventually displaced by a different cluster that

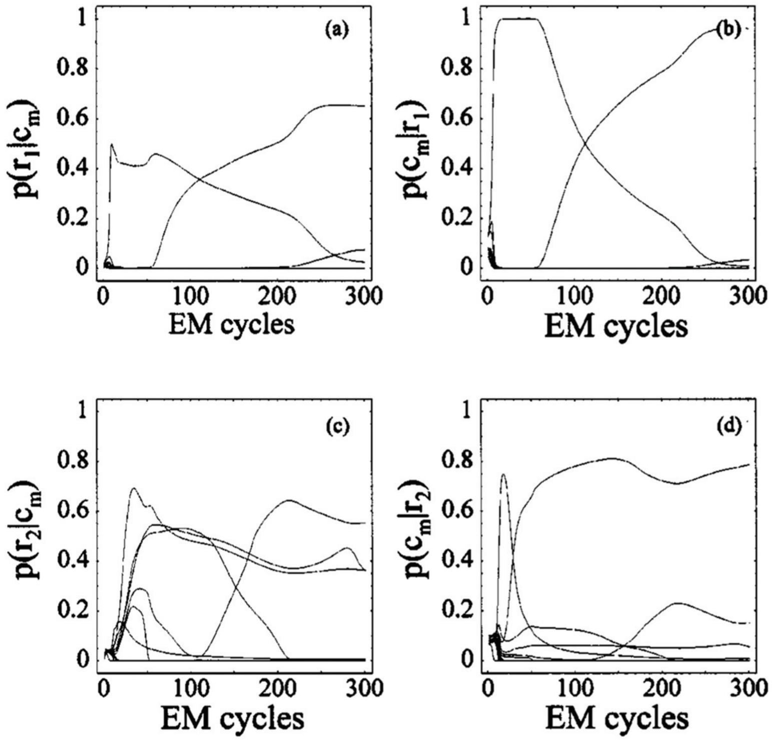

Figure 5.4. Plot (a) shows 16 separable forward probabilities at the tagged data point $\vec{r}_1$ as a function EM cycles. Plot (b) shows the corresponding posterior probabilities. Plots (c) and (d) depict the separable forward and posterior probabilities, respectively, at the data point at $\vec{r}_2$. Reprinted with permission from Ref. [82]. Copyright 2003 American Institute of Physics.

becomes nearly centered at $\vec{r}_1$. The situation for $\vec{r}_2$ is analogous to that for $\vec{r}_1$ but is complicated by the fact that there is greater overlap between multiple clusters. The forward and posterior probabilities at the point $\vec{r}_2$ are shown in Fig. 5.16c,d. Ultimately one cluster dominates the density estimate at $\vec{r}_2$; however, this is true to a lesser extent than at $\vec{r}_1$.

In Fig. 5.5 we plot the forward and posterior probabilities at $\vec{r}_1$ and $\vec{r}_2$ for the fully covariant model. It is clear that the behavior of the nonseparable Gaussian clusters is consistent with

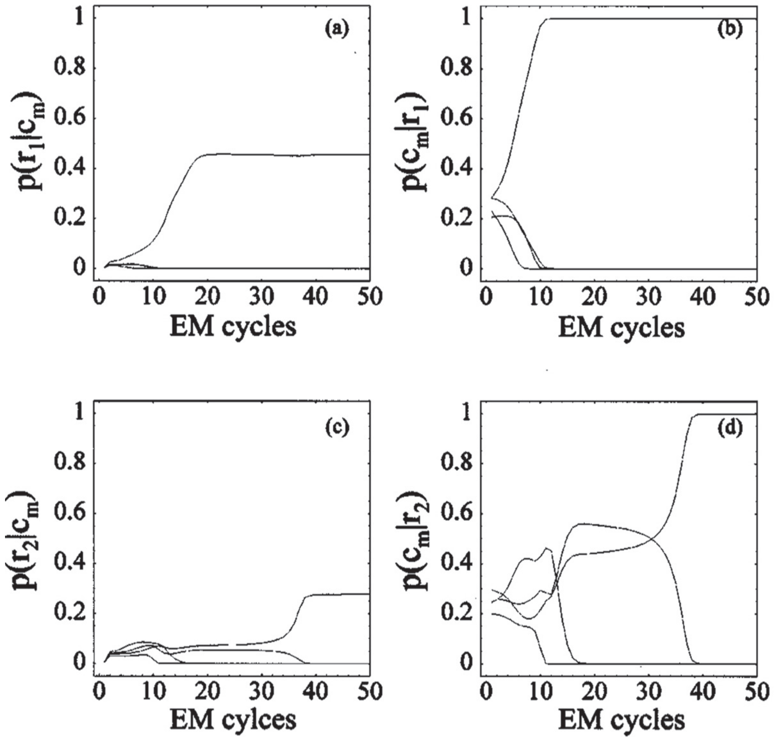

Figure 5.5. Plot (a) shows four nonseparable forward probabilities at the tagged data point $\vec{r}_1$ as a function EM cycles. Plot (b) shows the corresponding posterior probabilities. Plots (c) and (d) depict the four nonseparable forward and posterior probabilities, respectively, at the data point at $\vec{r}_2$. Reprinted with permission from Ref. [82]. Copyright 2003 American Institute of Physics.

the separable ones. The exception to this is that the fully covariant clusters converge to a stable configuration in fewer EM cycles. This is due to the obvious fact there are many more equally good arrangements for 16 nonseparable Gaussians than there are for only 4 nonseparable Gaussians. Another way of saying this is that the log-likelihood has many more local maxima for the $M = 16$ separable model compared to the $M = 4$ nonseparable model. This point is highlighted by Fig. 5.6, where we plot the log-likelihood L for several different density fits. The separable cases are designated

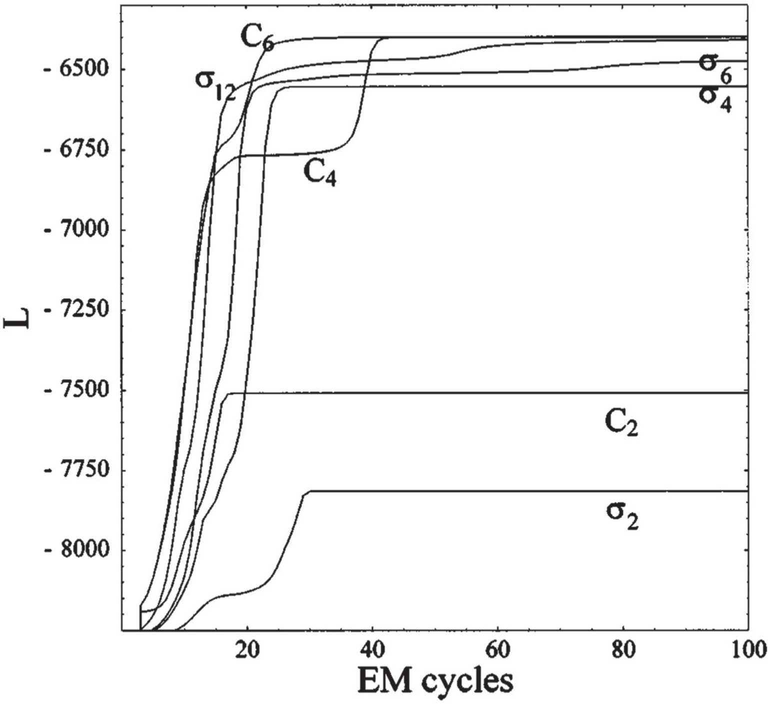

Figure 5.6. Plot of the log-likelihood verses number of EM cycles for various density estimates of the data illustrated in Fig. 5.15. The notation σ_m and C_m refers to a density fit performed with m Gaussian clusters using the separable and fully covariant model, respectively. Reprinted with permission from Ref. [82]. Copyright 2003 American Institute of Physics.

with a σ_m, where the integer m indicates how many Gaussians were used to perform the fit. Likewise, C_m refers to a fully covariant cluster fit with m nonseparable Gaussian components. The plateaus in the log-likelihood indicate that the EM algorithm is converging upon a root of the likelihood equation. It is conceivable that the EM algorithm could essentially become stuck at a local maximum or even a saddle point that does not give a particularly good density estimate. For these situations it is necessary to incorporate a small random perturbation in the cluster parameters in order to move the fit away from such anomalous regions of parameter space. Another problem is that a cluster might become too focused on a single data point. This is described as a root of the likelihood equation lying on the exterior of parameter space. When this happens, the variance and weight of the cluster become exceedingly small and in numerical applications will often round to zero, causing some terms in Eqs. (5.26)–(5.25) and (5.31)–(5.32) to diverge. This problem can be avoided in practice by adding a small fraction to the diagonal covariances in Eq. (5.32). This imposes an artificial boundary in parameter space that forces the Gaussian clusters away from the exterior roots.

5.2.4 *The ground state of methyl iodide*

Now that we have highlighted some key features of the mixture model approximation and EM algorithm, we turn our attention to a problem with more physical merits. In order to propagate the quantum ensemble in time we must compute both the classical and quantum forces acting on the ensemble particles. Given a maximum likelihood estimate for ρ in the form of Eq. (5.25) or (5.26), it is a fairly straightforward exercise in book-keeping to compute an approximate quantum force:

$$F_Q = \frac{\hbar}{4m}\left(\frac{\vec{\nabla}^3\rho}{\rho} - \frac{\vec{\nabla}(\vec{\nabla}\rho\cdot\vec{\nabla}\rho)}{2\rho^2} - \left(\frac{\vec{\nabla}^2\rho}{\rho} - \frac{\vec{\nabla}\rho\cdot\vec{\nabla}\rho}{\rho^2}\right)\frac{\vec{\nabla}\rho}{\rho}\right) \tag{5.37}$$

in terms of the Gaussian parameters. The quantum and classical forces are then used to drive the ensemble of trajectories by integrating Eqs. (5.17) and (5.18) over a short time step using a Verlet leapfrog-type method. The EM algorithm is repeated using the previously fit cluster parameters as the starting point. Recycling the old parameters significantly decreases the number of EM cycles required to obtain convergence in the next density estimate. The whole process of alternating between EM cycles and Verlet steps continues until we have integrated the equations of motion to some appropriate final time.

For a Gaussian density packet evolving on a parabolic potential surface, the mixture model approximation requires only one cluster and is exact for all time. For nontrivial problems, however, the quantum density will generally exhibit a very complicated structure in configuration space. Clearly, the mixture model approximation will not be able to capture the exact intricacies of a realistic quantum distribution. Consequently, it is not feasible, using the present formulation of our methodology, to obtain numerically accurate quantum densities for nonstationary systems. Ground state quantum densities, on the other hand, are characteristically much simpler than their excited state and nonstationary counterparts. We believe our approach will be most useful for determining the ground state properties of high-dimensional systems.

For stationary systems, the quantum force exactly counterbalances the classical force and the ensemble of quantum trajectories does not evolve in time. The ground state can then be realized from a nonstationary state by adding a small damping term to Eq. (5.17):

$$\dot{\vec{v}} = F_Q - \vec{\nabla} V/m - \gamma \vec{v} \tag{5.38}$$

where γ represents a small dissipative coefficient. This fictitious friction, in turn, causes the ensemble particles to lose a small amount of kinetic energy at each time step in the simulation. For a classical ensemble, the distribution collapses to a delta function centered about the minimum energy point(s) of the potential surface. For the quantum mechanical ensemble, however, as the distribution becomes increasingly narrow, the quantum force becomes very strong and requires the ensemble to maintain some minimum finite width. At longer simulation times an equilibrium is reached, and the resulting distribution is representative of the ground state quantum density. The corresponding ground state energy can be resolved to within the statistical error of a Monte Carlo integration over the ensemble elements.

To illustrate this, we demonstrate the convergence of an initial Gaussian ensemble to the ground state distribution for the CH_3-I stretching/bending modes of the lowest electronic state of methyl iodide. For our purposes this provides a nontrivial anharmonic potential surface to test our methodology. The vibrational system is treated as a single particle ($m = 20\ 000$ amu) evolving on a two-dimensional (2D) model potential energy surface developed by Shapiro and Bersohn [96]. The potential energy curves for this

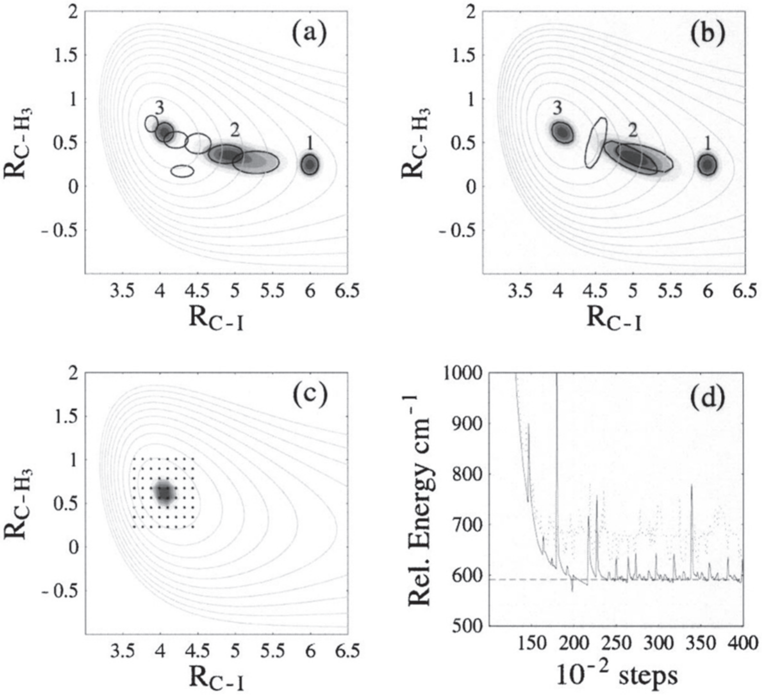

Figure 5.7. Plots (a) and (b) show the relaxation of a Gaussian wave packet in an anharmonic potential well for both the separable and fully covariant models, respectively. The gray contours reflect the potential energy curves for a model of CH_3I. The shaded contours indicate the shape of the approximated density after (1) 0, (2) 10 000, and (3) 40 000 Verlet time steps, respectively. The solid curves represent the half-width contours of the Gaussian clusters. Plot (c) shows the numerically accurate DVR ground state and the associated grid of quadrature points. Plot (d) shows the energy of the estimated density as a function of time steps. The dotted and solid data corresponds to the separable and nonseparable models, respectively, while the dashed horizontal line represents the DVR energy. Reprinted with permission from Ref. [82]. Copyright 2003 American Institute of Physics.

anharmonic surface are depicted in Fig. 5.7 by the gray contour lines. In Fig. 5.7a we illustrate a numerically exact representation of the ground state density obtained by diagonalizing the Hamiltonian of the system using a 2D discrete variable representation (DVR). The grid points indicate the minimum number of Chebychev quadrature points required to obtain convergence in the lowest-energy eigenvalue. Obviously, a much larger grid would be necessary to perform a dynamical calculation on this system.

Fig. 5.7b,c illustrates the estimated density for both the separable and fully covariant models, respectively. The black ovals represent the half-width contours of the Gaussian clusters. There are four clusters in the separable case and two for the fully covariant model. The various contour plots labeled (1), (2), and (3) correspond to snapshots of the estimated density at different points in the simulation. For both models, the initial density (1) is Gaussian, and all but one of the clusters are redundant. As the ensemble is propagated the individual clusters behave differently from one another. The contours (2) show the quantum density at an intermediate time after roughly 10 000 Verlet time steps ($\delta t = 1$ atomic time unit). At longer times an equilibrium is achieved and the contours (3) are representative of the quantum ground state. In Fig. 5.7d we plot the energy of the system relative to the bottom of the potential well as a function of the number of Verlet time steps. The DVR energy at 591 cm^{-1} serves as a benchmark and is indicated by the dashed horizontal line. The dotted and solid energy curves are for the separable and nonseparable models, respectively. Dropping the first 20 000 time steps, we find that the average energy for the separable case is 665.2 ± 33.6 cm^{-1}, which is well above the DVR energy. The average energy for the nonseparable model falls just barely within reach of the DVR energy at 580.0 ± 10.1 cm^{-1}. The sharp energy spikes for the nonseparable calculation are due to anomalous changes in the cluster parameters, such as a sudden jump in μ_m or rotation of C_m. These effects do not pose a significant problem since the clusters quickly respond to correct the abnormalities within a few time steps. For the sake of comparison we have also performed the same calculation for a mixture model with four fully covariant clusters. The average energy for the equilibrated system improved only slightly, but the statistical variation doubled 581.6 ± 21.7 cm^{-1}. The final arrangements of the clusters for the $M = 2$ and $M = 4$ covariant models are not discernible, and the additional clusters do not significantly aid or disrupt the global density fit. However, they do contribute to the sporadic deviations in the equilibrium energy.

In the following sections we present some of our work in applying this approach to study the thermodynamic properties of mesoscopic rare-gas clusters and conclude by presenting an extension for computing excitation energies.

5.3 Quantum Effects in Atomic Clusters at Finite Temperature

Rare-gas clusters approximated by the simple LJ pair-wise potential are ideal test cases for many-body simulations [10, 79, 93], providing a useful benchmark for new methods. In addition, rare-gas clusters are often used to probe the transition from microscopic to macroscopic properties in atomic systems. The mesoscopic regime has many unique properties

In this section, we extend the quantum hydrodynamic method developed in the previous section [37] to study the nature of quantum effects for mesoscopic systems at finite temperature through the entropic functional given by Mermin [88]. Our approach assumes that the configurational density $n(\vec{r}_1, \ldots, \vec{r}_N)$ can be represented with a superposition of statistical approximates, $p(\mathrm{r}_1, \ldots, \vec{r}_N, c_m)$. The algorithm then uses a Bayesian analysis to determine the best statistical approximates given a statistical sampling of the density. It then uses a grid-free hydrodynamic adaptive approach to relax sample points that make up a statistical sampling of the quantum density to the ground state equilibrium density.

In what follows, we present a brief overview of the grid-free adaptive hydrodynamic approach for computing the quantum ground state density for a system of N nuclei introduced earlier and then show how it can be extended to finite temperature. We also give a review of the Bayesian analysis used to deduce the best set of m statistical approximates from a statistical sampling of the density. We then show the quantum hydrodynamical scheme used to adapt the sample points toward a minimal energy configuration. We will then present results on clusters of neon of up to 37 atoms ($N = 37$) for temperatures from 0 K to 30 K, which spans the solid to liquid transition for bulk Ne ($T_m = 24.56$ K and $T_b = 27.07$ K). In the present work we will demonstrate that quantum effects can indeed be captured with our hydrodynamic method at finite temperature and that quantum effects lead to some thermodynamic behavior for small, symmetric clusters.

5.4 Quantum Structures at Zero and Finite Temperature

5.4.1 *Zero temperature theory*

The Euler–Lagrange equation for the motion of our particles is then derived with the help of the hydrodynamic description of quantum mechanics. We begin by specifying the full many-body Hamiltonian and will follow along similarly to density functional theory (DFT) [92]. The potential corresponds to the nuclear motion of a collection of atoms with pair-wise interaction potentials.

$$H = -\sum_{i=1}^{N} \frac{1}{2m_i} \vec{\nabla}_i^2 + \sum_{i \neq j} V(ij) \tag{5.39}$$

where the first is the sum of the kinetic energies of the individual atoms and the second is the sum of the potential energy contributions. $\vec{r}_i$ is the vector location of atom i, and n_i is the corresponding density. We also have an arbitrary N-body trial density given by:

$$n(\vec{r}) = \sum_i n_i(\vec{r}_i) \tag{5.40}$$

The energy functional corresponding to this density and Hamiltonian is given by:

$$E[n] = T[n] + \sum_{i \neq j} \int \int n_i(\vec{r}_i) n_j(\vec{r}_j) V(ij) d\vec{r}_i d\vec{r}_j \tag{5.41}$$

The kinetic energy operator is separable since we have assumed distinguishability among the constituent atoms. Therefore, the kinetic energy term is the sum of the individual kinetic energy functionals.

$$T[n(1 \cdots N)] = \sum_{i=1}^{N} T_i[n_i(\vec{r}_i)] \tag{5.42}$$

As in electronic structure DFT, evaluating the kinetic energy functionals is problematic since evaluating the quantum kinetic energy is a nonlocal operator and the density is a local function [92].

If instead we write the quantum wave function in polar form, as in the hydrodynamic formulation of QM [31, 33, 83] and also in the time-dependent DFT formulation [6, 7]:

$$\Psi(\vec{r}) = \sqrt{n(\vec{r})}e^{i\phi(\vec{r})} \tag{5.43}$$

we can arrive at a stationary condition that if $\vec{\nabla}\phi = 0$[52],

$$V(1\cdots N) - \sum_i \frac{1}{2m_i}\frac{1}{\sqrt{n_i(\vec{r}_i)}}\nabla_i^2\sqrt{n_i(\vec{r}_i)} = const \tag{5.44}$$

at all points in space. The constant is the energy of the system. We note here the similarity of the second term in the previous equation with the quantum force from diffusion Monte Carlo, $\vec{\nabla}\psi/\psi$. This term is also known as the quantum potential in the Bohm formulation. By inspection, then, we can define our kinetic energy functional as:

$$T[n(\vec{r}_i)] = -\frac{1}{2m_i}\int\sqrt{n_i(\vec{r}_i)}\nabla_i^2\sqrt{n_i(\vec{r}_i)}d\vec{r}_i \tag{5.45}$$

Integrating by parts and taking $n(i) \rightarrow 0$ at $\pm\infty$ produces the familiar von Weizsacker kinetic energy functional [101]:

$$T_W[n(\vec{r}_i)] = +\frac{1}{8m}\int\frac{1}{n_i(\vec{r}_i)}\vec{\nabla}_i n_i(\vec{r}_i)\cdot\vec{\nabla}_i n_i(\vec{r}_i)d\vec{r}_i \tag{5.46}$$

Thus, the total energy functional is given in terms of the single-particle densities.

$$E[n] = \sum_{i=1}^{N} T_W[n_i(\vec{r}_i)] + \sum_{i\neq j}\int\int n_i(\vec{r}_i)n_i(\vec{r}_j)V(ij)d\vec{r}_i d\vec{r}_j \tag{5.47}$$

Taking the variation of $E[n]$ with respect to the single-particle densities with the constraint that $\sum_i\int n_i(\vec{r}_i)di = N$:

$$\delta\left\{\sum_{i=1}^{N}\left[T_W[n_i(\vec{r}_i)] + \sum_{j\neq i}\int\int n_i(\vec{r}_i)n_j(\vec{r}_j)V(ij)d\vec{r}_i d\vec{r}_j - \mu\left(\int n_i(\vec{r}_i)d\vec{r}_i - 1\right)\right]\right\} = 0 \tag{5.48}$$

leads to the following Euler–Lagrange equations:

$$\frac{\delta T_W[n_i(\vec{r}_i)]}{\delta n_i(\vec{r}_i)} + \sum_{j\neq i}\int V(ij)n_j(\vec{r}_j)d\vec{r}_j - \mu = 0 \tag{5.49}$$

When satisfied, μ is the vibrational ground state energy, and the $n_i(\vec{r}_i) = |\phi_i(i)|^2$ are the probability densities of the individual nuclei. This leads to an effective mean field potential for each atom of the form:

$$V_i^e = Q(\vec{r}_i) + V_e(\vec{r}_i) + \sum_{j=1}^{N} V_p(\mathrm{r}_i, \vec{r}_j) \tag{5.50}$$

Here, $Q(\vec{r})$ is the quantum potential, $V_e(\vec{r}_i)$ is an external potential, which corresponds to any external driving field ($V_e = 0$ in the present study), and $V_p(\vec{r}_i, \vec{r}_j)$ is the pair-wise interatomic interaction potential.

5.4.2 *Finite temperature theory*

An extension of Hohenberg–Kohn theorem to finite temperatures was reported a number of years ago by Mermin [88, 111]. For a system at finite temperature under the conditions of a grand ensemble, $Z(T, V, \mu) = \mathrm{Tr}\{e^{-\beta(H-\mu N)}\}$, an equilibrium state density matrix will minimize Ω, the grand potential. This is given by:

$$\Omega = -\frac{1}{\beta}\ln(\mathrm{Tr}\{e^{-\beta(H-\mu N)}\}) \tag{5.51}$$

where H is the Hamiltonian, N the number operator, and μ the chemical potential. Nearly 40 years ago, Mermin [88] showed that by writing Ω as a functional of an arbitrary trial density matrix:

$$\Omega[\hat{\rho}_T] = \mathrm{Tr}\{\hat{\rho}_T(K + V - \mu N + \frac{1}{\beta}\ln\hat{\rho}_T)\} \tag{5.52}$$

$\delta\Omega = 0$ only if the correct density matrix is used. Thus, for any trial density matrix $\hat{\rho}_T \neq \hat{\rho}$, then $\Omega[\hat{\rho}_T] \geq \Omega[\hat{\rho}]$. Mermin also shows that there is a unique density associated with the equilibrium density matrix, $n(\vec{r}) = tr\{\hat{\rho}|\psi(\vec{r})|^2\}$. This implies then that one can write the grand potential as a functional of the density:

$$\Omega[n(\vec{r})] = F[n(\vec{r})] - \mu \int n(\vec{r})d\vec{r} \tag{5.53}$$

where our free energy functional $F[n]$ is given by:

$$F[n(\vec{r})] = \mathrm{Tr}\{\hat{\rho}[n(\vec{r})](K + V + \frac{1}{\beta}\ln\hat{\rho}[n(\vec{r})])\} \tag{5.54}$$

$$= T_w[n(\vec{r})] + V[n(\vec{r})] + \frac{1}{\beta}S[n(\vec{r})] \tag{5.55}$$

Here we have made the substitution of $S[n(\vec{r})]$ for the entropic term. The T_w functional is the Weizsacker functional, which along with the potential functional, is identical to our previous work [37] as well as Sec. 5.4.1. We have excluded exchange and correlation terms since we have assumed noninteracting particles. The inverse temperature, β, is a Lagrange multiplier used in the determination of the ground state density. This is similar to the chemical potential used previously in the determination of the ground state at $T = 0$. The minimum of the Ω functional will correspond to the atomic density profile of the system at a given temperature. Note that the free energy functional, $F[n]$, contains the kinetic energy and external potential operators as well as an entropy/temperature term so that now the stationary equilibrium state will be an energetic compromise between the quantum and the entropic potentials, both of which tend to destabilize the clusters, and a mean field interaction potential that tends to stabilize the clusters. The net effect is that as the cluster temperature increases, the clusters will be increasingly unstable and undergo transitions from ordered to disorded states.

Since Eq. 5.52 corresponds to the grand

$$\Omega = E - TS - \mu N \tag{5.56}$$

we are trivially obeying the relation $S = (\partial\Omega/\partial T)$. The thermodynamic justification for the form of the entropic functional defined by Mermin can be seen from the form of the entropy in Boltzmann's eulogistic equation:

$$S = k_B \ln(\Omega_{mc}) \tag{5.57}$$

where Ω_{mc} is the microcanonical density of states. Since we can write the microcanonical density of states in terms of the density matrix in the von Neumann definition of entropy, we can write the above equation as:

$$S = -k_B \mathrm{Tr}\{\hat{\rho}\ln(\hat{\rho})\} \tag{5.58}$$

This is also sometimes called differential entropy. The entropic functional takes into account the contribution from temperature-entropy work into our energy functional, and the β problem of path integral based approaches is avoided.

We can minimize Ω to obtain the chemical potential:

$$\mu = \frac{1}{\beta}\frac{\delta S[n]}{\delta n(\vec{r})} + Q(\vec{r}) + V_{ext}(\vec{r}) \tag{5.59}$$

Again Q is the quantum potential derived from the functional derivative of the Weizsacker term, $Q = \delta T[n]/\delta n$, and in a similar manner V is simply the mean field potential of a given atom in terms of all the other atoms. Now all that remains is to calculate this iteratively as before with a temperature correction related to $S[n(\vec{r})]$.

We assume that the entropic contribution is additive and can be derived using the von Neumann entropy:

$$S[n(\vec{r})] = \frac{1}{\beta}\sum_i \int n_i(\vec{r}_i)\ln(n_i(\vec{r}_i))d\vec{r}_i = \sum_i S[n(i)] \tag{5.60}$$

where the sum is over individual atoms. Taking the functional derivative with respect to the density, needed in the equations of motion of the particles, we define an “entropic force” as:

$$\frac{\delta S[n(\vec{r})]}{\delta n_i} = \frac{1}{\beta}(\ln(n_i(\vec{r}_i)) + 1) \tag{5.61}$$

In order to test our assumption and verify its range of applicability, we consider a simple harmonic system with a normalized Gaussian density function:

$$n(x) = \sqrt{\frac{a}{\pi}}e^{-x^2/2\langle x^2\rangle} \tag{5.62}$$

As such, the free energy is given by (with $\hbar = 1$):

$$\langle F\rangle = \frac{1}{8m\langle x^2\rangle} + \frac{m\omega^2}{2}\langle x^2\rangle - \frac{1}{2\beta}\left(\ln(2\pi\langle x^2\rangle) + 1)\right) \tag{5.63}$$

The first two terms are simply the average kinetic and potential energies. The last term is temperature dependent (since $\beta = 1/k_BT$) and arises from the entropy contribution. Minimizing $\langle F\rangle$ with respect to a yields an optimal width parameter of:

$$\langle x^2\rangle_{opt} = \frac{k_BT}{2m\omega^2}\left(1 + \sqrt{1 + (\hbar\omega/k_BT)^2}\right) \tag{5.64}$$

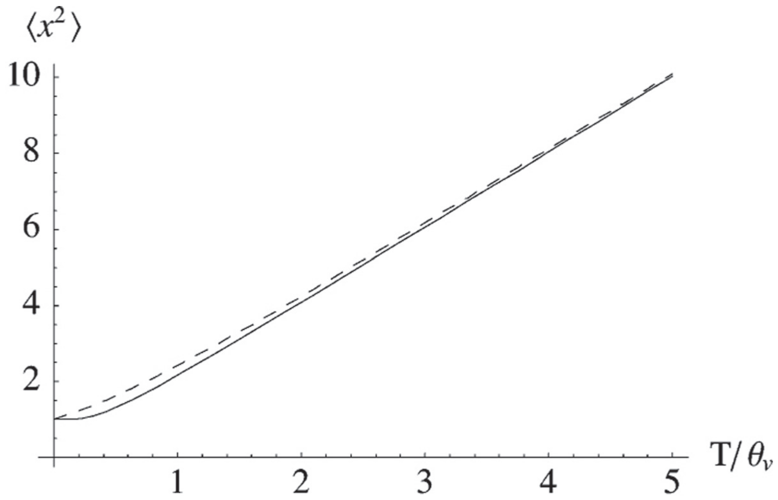

Figure 5.8. $\langle x^2 \rangle$ vs. T comparing the approximate entropy functional of Eq. 5.60 (- - -) to the exact (—) value for a harmonic system at finite temperature. Reprinted with permission from Ref. [36]. Copyright 2007 American Chemical Society.

For comparison the exact expression for the width of a harmonic oscillator at finite temperature is [40]:

$$\langle x^2 \rangle_{\text{exact}} = \frac{\hbar}{2m\omega} \coth\left(\frac{\Theta_v}{2T}\right) \tag{5.65}$$

where $\Theta_v = \hbar\omega/k_B$ is the vibrational temperature.

In Fig. 5.8 we compare our approximation for $\langle x^2 \rangle$ against its exact value for a system with $m = 1$ and $\omega = 1$ with all constants in atomic units. At high temperature, we recover the correct limiting behavior of the width. Significant deviation between the analytical density matrix value of $\langle x^2 \rangle$ and that for hydrodynamic approach is only seen for $\omega \gg 1$. Based upon a normal mode analysis of Ne_{13}, these clusters have values for ω that are typically on the order of $O(10)\text{cm}^{-1}$. In atomic units this corresponds to a frequency on the order of $\omega \approx O(10^{-6})$ so that excellent agreement can be expected for the systems examined. In general, at temperatures below $2\hbar\omega/k_B$ there is slight disagreement, but we do recover the correct $T = 0$ value. Consequently, the Mermin functional utilized in the present work will introduce systematic error into our results; however, we anticipate this to be quite minimal.

5.4.2.1 Computational approach: The mixture model

In order to utilize the hydrodynamic description one needs a quantitative description of the density. This will be done directly from an ensemble of points sampled from the initial quantum density in the following way. To begin, the single-particle probability distribution functions (PDF) can be represented by a mixture model [45, 87] by summing a finite number M of density approximates:

$$n(\vec{r}) = \sum_{m}^{M} p(\vec{r}, c_m) \tag{5.66}$$

where $p(\vec{r}, cm)$ is the probability that a randomly chosen member of the ensemble has the configuration $\vec{r}$ and is a variant of the mth approximate designated by c_m. These approximates may be Gaussians or any other integrable multidimensional function, which can be parameterized by its moments. For Gaussian clusters, we have a weight $p(c_m)$, a mean position vector μ_m, and a covariance matrix C_m.

By definition, each joint probability in Eq. 5.66 is related to a pair of conditional probabilities according to the relation:

$$p(\vec{r}, c_m) = p(c_m)p(\vec{r}|c_m) = n(\vec{r})p(c_m|\vec{r}) \tag{5.67}$$

The forward conditional probability $p(\vec{r}|c_m)$ refers to the probability that a randomly chosen variant of c_m has the configuration $\vec{r}$, and the posterior probability $p(c_m|\mathrm{r})$ refers to the probability that the configuration point $\vec{r}$ is a variant of the approximate c_m. Notice, $n(\vec{r})$ and $p(c_m)$ are the quantum density and weight of the mth approximate, respectively.

As shown in our previous works [37, 82], this formulation can be used to define a multidimensional quantum density with user-defined amounts of correlation between the particles. Briefly we can outline our procedure as follows. With a Gaussian model representing the full $3N$ dimensional system:

$$p(\vec{r}|c_m) = \sqrt{\frac{\|\mathrm{C}^{-1}\|}{(2\pi)^{N_d}}} e^{(\vec{r}_d - \mu_{m,d}).\mathrm{C}_m^{-1}.(r_d - \mu_{m,d})} \tag{5.68}$$

the covariance matrix, **C**, can be used to eliminate (or maintain) coupling between various degrees of freedom. Then one must determine the Gaussian parameters $p(c_m)$, μ_m, and C_m, which define the density. This is facilitated using an iterative EM algorithm. In each case, these are readily approximated by summing over an ensemble of points $\{\vec{r}_n\}$ sampled from the $n(\vec{r})$ or probability distribution function. For instance, the mean positions are approximated with:

$$\vec{\mu}_m \approx \frac{1}{Np(c_m)} \sum_{n}^{N} \vec{r}_n \, p(c_m|\vec{r}_n) \tag{5.69}$$

The updated Gaussian parameters are then used to update the posterior terms $p(c_m|\vec{r}_n)$ for each $\vec{r}_n$ sample point by inserting this back into Eq. 5.68 and using Bayes's equation:

$$p(c_m|\vec{r}_n) = \frac{p(c_m)\,p(\vec{r}_n|c_m)}{\sum_m p(c_m)\,p(\vec{r}_n|c_m)} \tag{5.70}$$

This procedure progressively solves for the best set of parameters, given a distribution of sample points.

The EM algorithm described above allows us to generate an approximate analytical functional form for the single-particle density via statistical sampling over an ensemble of points. The next step is to adjust the single-particle densities themselves to produce a lower total energy. We do this by deriving the quantum hydrodynamic equations of motion for the sample points, $\vec{r}_{in}$, where i labels a given atom and n labels a given sample point associated with density $n_i(\vec{r})$.

5.4.2.2 Computational approach: Equations of motion for the sample points

The quantum Hamilton–Jacobi equation generates the equations of motion for the ray lines of a time-dependent solution to the Schrödinger equation [15, 16, 18, 110]. This allows convergence to the ground state by relaxing along an action field determined for each atom. This gives a set of time-dependent, self-consistent field equations whereby the motion of atom i is determined by the average potential interaction between atom i and the rest of the atoms in the system.

$$\dot{S}_i(\vec{r}) + \frac{|\vec{\nabla}_i S|^2}{2m_i} + \sum_{j \neq i} \int V(ij) n_j(\vec{r}) d\vec{r} \\ - \frac{1}{2m_i} \frac{1}{\sqrt{n_i(\vec{r})}} \nabla_i^2 \sqrt{n_i(\vec{r})} + \frac{1}{\beta} \int n_i(\vec{r}) \ln(n_i(\vec{r})) = 0 \quad (5.71)$$

Taking $\vec{\nabla} S = \mathrm{p}$ as a momentum of a particle, the equations of motion along a given ray line or sample particle $\mathrm{r}_{\mathrm{in}}(t)$ of the quantum wave function are given by:

$$m_i \ddot{\vec{r}}_{in} = -\sum_{j \neq i} \int (\vec{\nabla}_i V(ij)) n(\vec{r}_j) d\vec{r}_j - \vec{\nabla}_i Q[n(\vec{r}_i)] + \vec{\nabla}_i \frac{\delta S[n(i)]}{\delta n_i} \quad (5.72)$$

where $Q[n(i)]$ is the Bohmian quantum potential specified by the last term in Eq. 5.71. Stationary solutions of the time-dependent Schrödinger equation are obtained whenever $m_i \ddot{\vec{r}}_n = 0$. Consequently, we reach the ground state by relaxing the sample points in a direction along the energy gradient:

$$\vec{\nabla}_i E = -\sum_{j \neq i} \int (\vec{\nabla}_i V(ij)) n_j(\vec{r}_j) d\vec{r}_j - \vec{\nabla}_i Q[n_i(\vec{r}_i)] + \vec{\nabla}_i \frac{\delta S[n(i)]}{\delta n_i} \quad (5.73)$$

keeping $n(\vec{r}_j)$ fixed. This generates a *new* statistical sampling that we then use to determine a new set of approximates and the process is repeated.

The algorithm can be summarized as follows:

(1) For each atom, generate and sample a normalized trial density $n_i(\vec{r}_i)$.
(2) Using the EM routines and the given sample of points, compute the coefficients for the density approximates.
(3) Compute the forces on each point using Eq. 5.71 and advance each point along the energy gradient for one “time” step, either discarding or dampening the velocity of each point. This generates a new sample of points describing the single-particle density for each atom. The new distribution should have a lower total energy since we moved the sample points in the direction toward lower energy.

Iterating through these last two steps, we rapidly converge toward the global quantum energy minimum of the system.

5.4.3 *Computational studies*

5.4.3.1 Zero temperature results

In all the calculations presented here, we used 100 statistical points to represent the density of each atom and propagated the SCF equations described above until the energy and the density were sufficiently converged. To reach convergence, this typically required a few hundred thousand iterations. The LJ parameters used for the neon atoms are $\epsilon = 0.3059$ kJ/mole and $\sigma = 2.79$ Å [76]. The initial centers of the Gaussian approximates correspond to the position of the global energy minima for each cluster with initial widths taken from a harmonic oscillator approximation.

The primary motivation for continuing the study of these clusters at zero temperature is the desire to be able to simulate the quantum dynamics of bulk systems. In our previous work [37], we were limited to systems with less than 20 atoms. Subsequent improvement of our algorithms has allowed us to substantially advance past this limit. Furthermore, it is recognized that roughly 110 atoms per unit cell are required to approximate the bulk behavior of many-cluster systems [97]. Even so, our current computational resources limited us to clusters with up to 85 atoms at $T = 0$ K and roughly half this at higher temperatures.

Our $T = 0$ K results are summarized in Fig. 5.9, which shows the various contributions to the total energy. First, we note that the contribution from the quantum potential (average kinetic energy) increases monotonically with system size. Moreover, the total energy $\langle E \rangle$ decreases monotonically. This is to be expected since the larger clusters have increasingly more nearest-neighbor interactions as the size of the system increases.

In Fig. 5.9 we also compare the present results to a similar semiclassical study by Calvo *et al.* [24]. In their results the zero-point energy of the static structure of the global minimum was calculated and then added in an ad hoc fashion to the pair-potential interaction. Generally, our results lie somewhat lower in total energy than

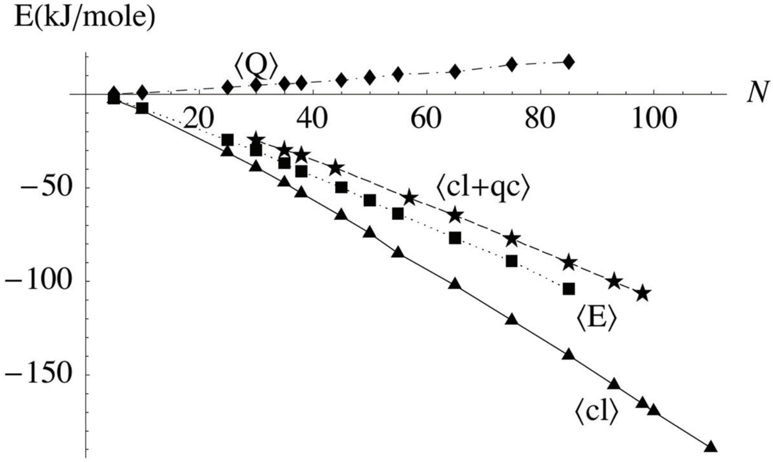

Figure 5.9. Various energetic contributions for quantum and classical neon clusters versus cluster size, N. Key: ⟨cl⟩ = classical global potential minimum energy, ⟨cl+qc⟩ = zero-point energy corrections from Ref. [24], ⟨E⟩ = total energy, ⟨Q⟩ = quantum kinetic energy (from quantum potential). Reprinted with permission from Ref. [36]. Copyright 2007 American Chemical Society.

the semiclassical estimates but above the classical global energy minimum for each cluster. We do note, however, that the inclusion of the quantum potential alters the total energy surface. Consequently, in some cases, the system could relax to a different minimum or in a superposition of close-lying minima due to tunneling. The clustering model can handle this situation through the inclusion of multiple Gaussian approximates for each atom. However, in each case examined here, we did not observe serious deviations or tunneling between nearly degenerate structures.

However, it is possible that the inclusion of quantum delocalization can influence the energetic ordering of nearly equivalent structures. Calvo *et al.* also investigated changes in the ground state structure as a result of quantum delocalization. They did this using a basin-hopping Monte Carlo optimization algorithm to explore the energy landscape of small Ne clusters with less than 100 atoms. In this study the zero-point energy contributions were again approximated in an ad hoc fashion similar to that shown in

Table 5.1. Ground state vibrational energies for Ne_n clusters for our results compared with the results tabulated by Calvo *et al.* (Ref. [24])

Cluster	order	Energy (From Ref. [24])	order	This work
17C	(1)	−11.0853 kJ/mol	(2)	−16.6336 kJ/mol
17B	(2)	−11.0814	(3)	−16.3188
17A	(3)	−11.0633	(1)	−16.6699
27B	(1)	−21.5483	(2)	−27.6994
27A	(2)	−21.5099	(1)	−28.2823
28B	(1)	−22.5892	(2)	−28.7459
28A	(2)	−22.5496	(1)	−29.3524

Adapted with permission from Ref. [36]. Copyright 2007 American Chemical Society.

Fig. 5.9. This can be summarized with the following: An initial Monte Carlo search over the potential energy hypersurface is performed to determine a test configuration. The zero-point energy of this test configuration is determined using the static atomic positions. The calculated zero-point energy is then added to the classical potential energy, and this sum is used for the Metropolis acceptance criteria. This process is repeated until the lowest-energy configuration is determined, now including both the pair-potential and the zero-point energy.

In our study as well as that from Ref. [24], the starting configurations were based upon the global classical minimum on the potential energy hypersurface of the cluster. In Calvo *et al.*'s semiclassical results, quantum effects produced a different global minimum for 35 of 99 cases for Ne_n in the range of $n \leq 100$. For example, the 17-atom cluster has three nearly equivalent minima (17A, 17B, and 17C) with energies $E_C < E_B < E_A$ separated by substantial potential barriers. Likewise, $n = 27$ and $n = 28$ each has two energetically similar minima. The energies (from Ref. [24]) of these are given in Table 5.1. The geometries of representative clusters discussed in this section are shown in Fig. 5.10. Remarkably, our results show a different ordering of the energies of these structures compared with the semiclassical results. The difference between the two results is consistent with the general trend shown in Fig. 5.9 and corresponds to the different levels of theory used in

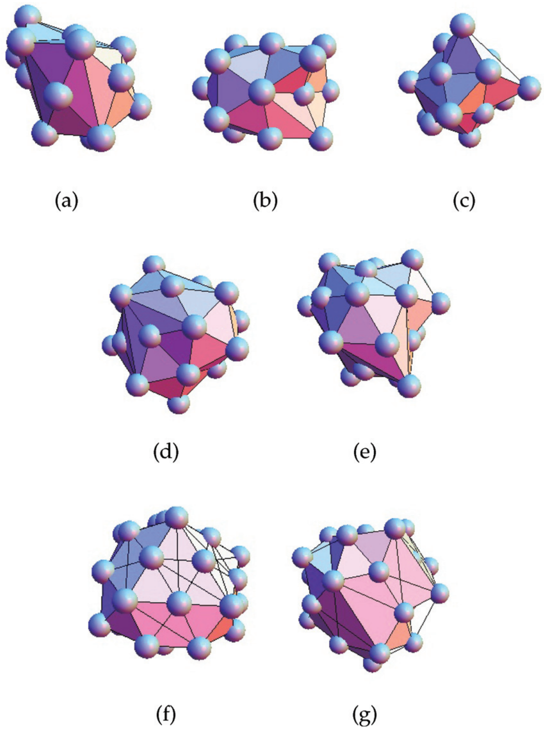

Figure 5.10. Minimal-energy LJ clusters from the Cambridge Cluster database. (http://www-wales.ch.cam.ac.uk) Point group is given in parenthesis. a: 17a (C_2), b: 17b (C_1), c: 17c (C_{3v}), d: 27a (C_{2v}), e: 27b (C_s), f: 37a (C_1), g: 37b (C_1).

each study. In the semiclassical approach, zero-point contributions are estimated from the curvature of the potential, *after-energy relaxation*, on the *potential* energy hypersurface. However, in our approach the quantum delocalization self-consistently *alters* the $3N$-dimensional *total* energy hypersurface being sampled.

The effects from quantum delocalization were approximated by using the structure's pair-potential value as well as the zero-point energy contribution inserted in an ad hoc manner to the Metropolis acceptance probability of the sampling from the potential surface. The initial structures used were based upon the global classical minimum. We note that there could be slight differences in the ground state structures of the clusters compared in Fig. 5.9. This is because, although the initial atom positions used for the hydrodynamic simulations were also taken from the global classical minimum, the hydrodynamic approach has a slightly altered energy surface and could possibly relax to a new minimum. This is not expected to result in serious deviations in the structure for the sizes listed.

In Ref. [24] Calvo *et al.* also analyzed the lowest-energy structures using a global optimization algorithm but with zero-point energy added in an ad hoc fashion to see the changes the quantum delocalization would have on the different ground state structures compared with classical results. According to their results neon was heavily influenced by quantum affects and showed a different global minimum for 35 of 99 cases for Ne_n in the range of $n \leq 100$. They state:

> Although challenging, it would be interesting to verify these results (the structures and their energies) with more accurate quantum Monte Carlo calculations at $T = 0$. A reasonable test case would be the size $n = 17 \ldots$ [24]

We have done this for all three structures of 17 atoms as well as the two structures they identified for 27- and 28-atom clusters of neon. We summarize these results in Table 5.1. The different structures are identified with 17A, 17B, etc., and the orderings of the energies are identified in the columns, that is, the lowest-energy structure is labeled with (1) and so on. The important point shown in Table 5.1 is that the orderings of the energies are different. Note that the difference in energies between columns 2 and 3 is consistent with the general trend shown in Fig. 5.9 and corresponds to the different levels of theory used. We think that our calculations are consistent with the general statement that ground state structures will be altered depending on the quantum delocalization, but our results indicate that ad hoc techniques of correcting for quantum delocalization are insufficient for global optimization algorithms since the zero-point energy is added after the "relaxation" portion. This is because the quantum delocalization actually changes the $3N$-dimensional energy surface. The hydrodynamic method we have outlined might be used in conjunction with these global optimization algorithms for a more accurate picture of the quantum effects.

5.4.3.2 Finite temperature results

The thermodynamics of small mesoscale systems is of considerable interest since what are typically extensive variables (e.g., total energy, entropy, etc.) that scale monotonically with system size can exhibit anomalous behavior as the system size becomes small. Add to this the influences of quantum delocalization, and one anticipates the predicted thermodynamics of these system to exhibit behavior quite different from the bulk or even from a purely classical prediction.

One attractive way to introduce quantum corrections into an otherwise classical molecular dynamics or Monte Carlo simulation is through the use of an effective "quantum potential." Typically such effective potentials are expansions of the quantum partition function in powers of $\hbar$. The Feynman–Hibbs potential is derived by characterizing a quantum particle with a Gaussian that has a width equal to the thermal de Broglie length centered about the particle and accounts for the spread in density expected for quantum particles. Under these assumptions the partition function can be simplified, and with a Gaussian density the pair potential term would be evaluated as:

$$V(\vec{r}_{ij}) = \left(\frac{2\mu}{\pi\beta\hbar^2}\right)^{3/2} \int dR\, V(|r+R|) e^{-\frac{2\mu}{\beta\hbar^2}R^2} \tag{5.74}$$

with some reduced mass, μ. The effective potential can then be found by expanding about r and truncating at some convenient order.

$$V_{\text{eff}}(r) = V(r) + \frac{\hbar^2\beta}{24m} V''(r) \tag{5.75}$$

Such an approach was used by Calvo *et al.* in Ref. [24] in their very comprehensive survey of how quantum delocalization affects the structure and energetics of rare-gas clusters and as such provides a highly useful point of comparison for our approach. We do note that these expansions assume λ to be small (compared to the local variation in the potential), as per the semiclassical WKB

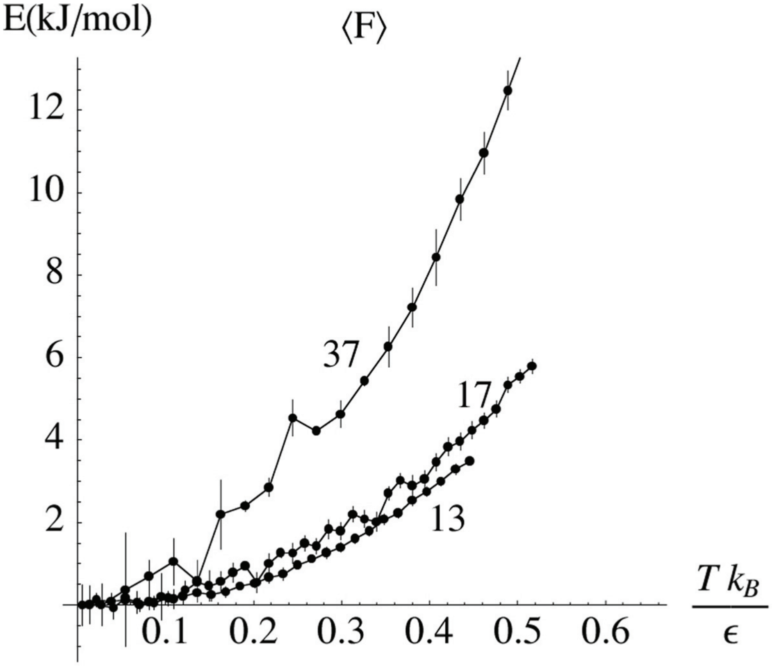

Figure 5.11. The free energy of the different clusters vs. reduced temperature $k_B T/\epsilon$. Error bars indicate numerical/statistical precision of each computed free-energy value. Note the $T = 0$ values are offset to a common origin for comparison. The energies at $T = 0$K for the three clusters are as follows: $F_0^{13} = -11.21$ kJ/mol, $F_0^{17} = -15.216$ kJ/mol, and $F_0^{37} = -39.03$kJ/mol. Reprinted with permission from Ref. [36]. Copyright 2007 American Chemical Society.

criteria. Consequently, for lower temperatures and higher degrees of quantum delocalization such effective quantum corrections are not applicable.

Here we focus on three clusters, Ne_{13}, Ne_{17}, and Ne_{37} over a temperature range spanning the solid to liquid transition for bulk Ne. In the figures that display the thermodynamic data, the temperature is given in terms of a reduced unit, which is the temperature in Kelvin multiplied by Boltzmann's constant and divided by the well depth of the LJ potential, $T' = Tk_B/\epsilon$. Figure 5.11 shows the total free energy (scaled to a common $T = 0$K origin) versus temperature for the three clusters. Figure 5.12 shows the

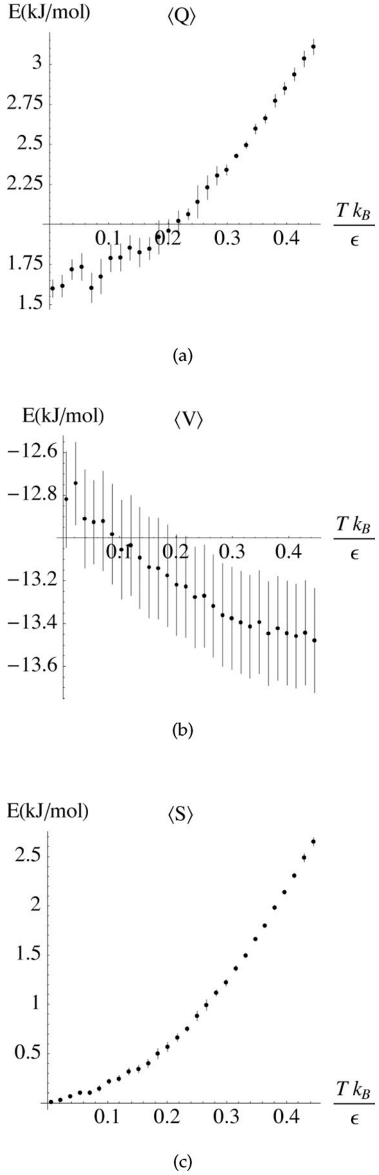

Figure 5.12. Plots of the quantum (a), total potential (b), and entropic (c) contributions to the total free energy vs. reduced temperature $k_B T/\epsilon$ for Ne_{13}. Reprinted with permission from Ref. [36]. Copyright 2007 American Chemical Society.

various contributions to the total free energy for the 13-atom cluster with similar behavior for the other clusters. First, the contribution from the quantum potential increases, as it should as T increases. The averaged quantum potential is simply the average quantum kinetic energy and as such is approximately inversely proportional to the de Broglie wavelength squared, $\langle Q \rangle \propto \lambda^{-2}$. Hence, $\langle Q \rangle$ increases as the system becomes more localized, corresponding to an increasingly shorter thermal de Broglie wavelength as T increases.

At higher temperatures, though, the quantum effects will be washed out as the de Broglie wavelength goes to zero. So, we expect that these factors will only be apparent at lower temperatures. The de Broglie wavelength is decreasing because the entropic potential causes an increase in the effective well depth that the atom feels with increasing T. As this happens, the cohesive forces increase in response to the decreased delocalization. This is a counterintuitive result since the cohesive forces are expected to decrease at higher temperatures. This results from the ability of atomic clusters to store energy as internal interaction energy rather than as kinetic energy. This aspect of mesoscopic clusters is discussed later.

It is useful to compare the results we have obtained with the analytical results obtained using the Debye model, which is known to have the correct low-temperature behavior for the heat capacity in the bulk material. The Debye model has a single adjustable parameter, the Debye temperature, defined by:

$$T_D = \frac{hc_s}{2k_B}\left(\frac{6N}{\pi V}\right)^{-3} \tag{5.76}$$

where $N/V = \rho$ is the bulk density and c_s is the speed of sound in the medium. From this we can derive the internal energy as:

$$U = 9Nk_B T(T/T_D)^3 \int_0^{T_D/T} \frac{x^3}{e^x - 1} dx \tag{5.77}$$

In general, T_D is determined by fitting the model to experimental thermodynamic data. For bulk Ne, $T_D = 75$ K.

Figure 5.13 compares the internal energy from our results to the Debye model with the Debye energy shifted so that it corresponds at $T = 0$ K with our results. By comparing the curves it is evident our results for the 17- and 37-atom systems will give similar Debye

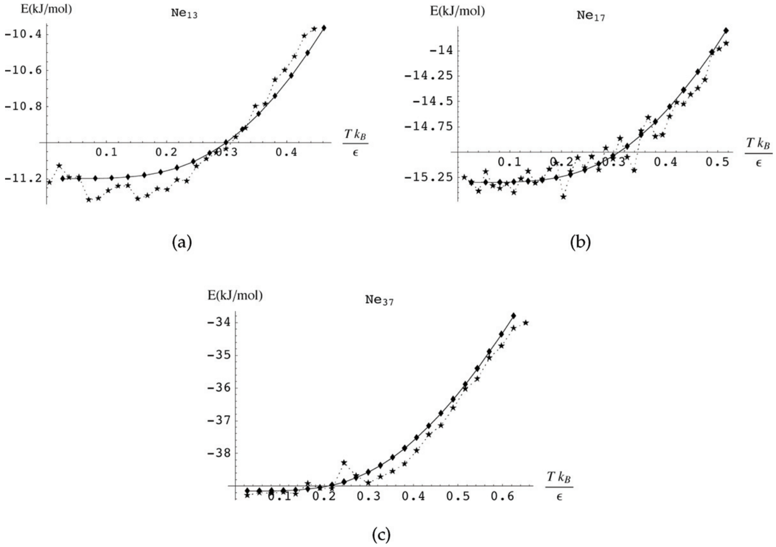

(a) (b)

(c)

Figure 5.13. Internal energy for various-sized clusters (· · ⋆ · ·) compared with the Debye model (—): (a) Ne_{13}, (b) Ne_{17}, and (c) Ne_{37}. Reprinted with permission from Ref. [36]. Copyright 2007 American Chemical Society.

temperatures to the bulk limit. The melting region can be identified as the nonlinear regions of the internal energy curves. In all three clusters, similar melting regions are observed for both approaches. It may seem remarkable that the Debye model is still useful, given the fact that these clusters are far from the bulk limit. However, the Debye model was constructed to account for both the high- and low-temperature caloric curves in condensed phase systems, and there is no fundamental problem with it as an approximation in this case.

Closer inspection of the internal energy curve for Ne_{13} indicates that tor temperatures, $0 < T \leq 0.2T'$, the internal energy *decreases* to some extent. This corresponds to a *negative heat capacity*. Even given a computational error estimate of $\pm$ 0.1 kJ/mole in the internal energy, the dip is clearly present in our results. This is not entirely unreasonable or unprecedented as several recent studies have predicted negative heat capacities for atomic clusters [14, 24, 66]. However, in Ref. [24] it was dismissed as an unphysical result. In addition negative heat capacities have also been observed recently for sodium clusters of 147 atoms [95] and they have been predicted in astrophysics, where energy can be added to a star whose temperature subsequently cools down [78]. Schmidt *et al.* [95] explain this for small atomic systems as a purely microscopic phenomenon. That is, for larger systems at a phase transition, energy is added as potential energy rather than kinetic energy so that the temperature remains constant over the course of the transition. For mesoscopic-scale atomic systems, on the other hand, it can be entropically favorable to avoid a partially melted state so that some energy is actually transferred from kinetic to potential energy, causing a negative heat capacity near phase transitions. Since this is not observed in classical simulations nor in the Debye model, it is possibly due to anharmonic quantum delocalization effects in the system. Another factor is that $N = 13$ and 147 clusters form complete icosohedral structures in their lowest-energy state. These are called magic-number clusters because of the stability of these highly symmetric forms. Since negative heat capacities have only been observed and/or predicted for magic-number clusters, this suggests that the negative heat capacity may be related to the symmetry of the system.

In all instances of negative heat capacity, the common factor is that the energy is not an extensive quantity and the interactions *between* subsystems must be taken into account. In the clusters we are examining, the temperature is raised but the atoms adjust themselves to store energy in the pair-potential interaction between atoms rather than increase the kinetic energy. Although this explanation offered by Schmidt *et al.* [95] appears to indicate that this is a purely classical effect; to our knowledge, no classical molecular dynamic methods have predicted negative heat capacities. Hence, we attribute the negative heat capacity to purely quantum mechanical effects in this system.

The reason for the failure of the Debye model for the smaller clusters is the continuous density of states for the phonons assumed by the model as seen in Eq. 5.77. As the clusters get smaller this becomes substantially different than the actual 3N-6 vibrational levels that the cluster contains. Though this is a powerful approximation, the levels very quickly become tightly packed and approach the continuous limit. If we loosely think of the portions of the density that are not adequately accounted for in this assumption as anharmonic regions, then our results indicate that these are important for describing the thermodynamics of these systems. Though we assume a Gaussian form for the statistical approximates used in the present work, which amounts to a harmonic approximation, we can sample the anharmonic regions of the density. This is because the statistical points themselves are free to sample the anharmonic regions. It happens that the anharmonic regions are more important for smaller clusters since they have more surface atoms and consequently experience more delocalization relative to the larger systems [37].

Based upon the above discussions we can say the thermodynamics of these clusters is influenced greatly by their relative ability to store energy, preferentially in the potential energy. This aspect of these systems can be studied by introducing a virial-like parameter consisting of the ratio of the quantum potential with the total internal energy, $\langle Q \rangle / \langle U \rangle$. This parameter essentially measures the percentage of energy contained in the kinetic energy. This will be given by:

$$\tau_m = -\frac{\langle Q \rangle}{\langle Q \rangle + \langle V \rangle}$$

τ_m should approach 1 as the temperature is raised, since the averaged quantum potential value is increasing with temperature and the averaged potential interaction energy should remain about constant, although the cluster will dissociate into a disordered state long before this point is reached. The averaged quantum potential value is a monotonically increasing function of the temperature because it is inversely proportional to the delocalization, or the de Broglie wavelength, $\langle Q \rangle \approx 1/\lambda^2 \approx T$. τ_m is shown for the three clusters in Fig. 5.14, and the curves clearly show that the smaller clusters must increase the amount of kinetic energy at a greater rate with temperature. Essentially the different rates of increase for τ_m are due to the larger clusters increased ability to store energy in the pair-potential. This explains the marked decrease in the temperatures of phase transitions as the size of the clusters drops.

Locating the melting point for mesoscopic systems is often a difficult task, even for systems with negligible quantum effects, because of the characteristic melting regions often seen for these systems.

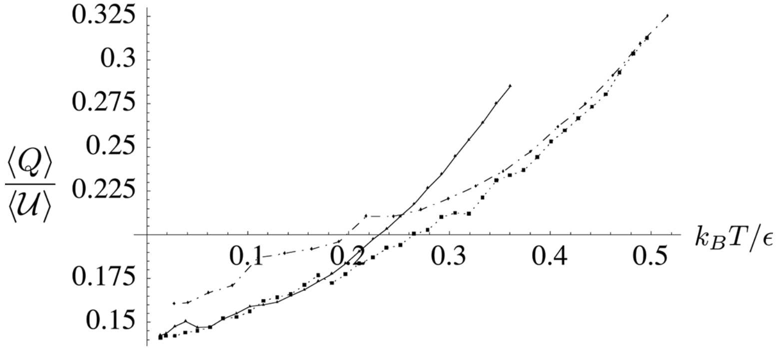

Figure 5.14. $(\langle Q\rangle/\langle U\rangle)$ vs. reduced temperature k_BT/ϵ. (Key: —: 13 atoms, $\cdots$:17 atoms, — · —: 37 atoms). Reprinted with permission from Ref. [36]. Copyright 2007 American Chemical Society.

Some factors that influence the melting characteristics of these clusters are the well depth for the lowest-energy configuration, the depths of the nearest neighbor wells around the ground state, and the time scales of the transitions [8]. A simple means of examining when melting has actually occurred is from the relative percentage of energy contained in the kinetic energy. In the bulk this will show a clear discontinuity at a phase transition and for microscopic or mesoscopic systems To analyze this possibility we introduce a virial-like term consisting of the ratio of the quantum potential with the total internal energy, $\langle Q\rangle/\langle U\rangle$, to help identify when melting has occurred. This is given by:

$$\tau_m = -\frac{\langle Q\rangle}{\langle Q\rangle + \langle V\rangle}$$

where we have taken the negative in order to have positive values for the parameter. τ_m should approach 1 as the temperature is raised, since the averaged quantum potential value is increasing with temperature, and the averaged potential interaction energy should remain about constant, but the cluster will dissociate into a disordered state long before this point is reached. The averaged quantum potential value is a monotonically increasing function of the temperature because it is inversely proportional to the delocalization, or the de Broglie wavelength, $\langle Q\rangle \approx 1/\lambda^2 \approx T$. τ_m is shown for all three cluster sizes examined at finite temperature in Fig. 5.14. These plots reveal some interesting aspects of these clusters. They show that the rate of increase of τ_m versus temperature is dependent on the cluster size, which explains the significant decrease in the phase transition temperatures observed for mesoscopic clusters compared to bulk values. The different rates of increase in τ_m for the different cluster sizes is due to the larger clusters' increased ability to store energy in the pair-potential.

5.5 Overcoming the Node Problem

One of the difficulties encountered in a quantum density-based scheme is that the quantum density is a positive quantity that vanishes whenever there is a node in the quantum wave function. The "node problem" has been a bugbear in the development of time-dependent quantum trajectory approaches and plagues Monte Carlo approaches. The difficulty within the quantum trajectory scheme is that when $\rho(x) \to 0$, the quantum potential becomes singular, giving rise to a sharply repulsive force that pushes sample points away from the node. One can adopt a "fixed-node" scheme to keep separate ensembles of sample points for each nodal region; however, this approach is not very flexible for high-dimensional systems, which may have nodal hypersurfaces.

We present here an idea we developed that uses supersymmetric (SUSY) QM within the context of a quantum Monte Carlo scheme to get around the node issue. By using the fact that SUSY QM gives rises to a series of isospectral Hamiltonians, we show that Monte Carlo ground state calculations in the SUSY partners can be used to reconstruct accurately both the spectrum and th estates of an arbitrary Schrödinger equation. Since the ground state of each partner potential is nodeless, we avoid any node problem typically associated with the Monte Carlo technique. While we provide an example of using this approach to determine the tunneling states in a double-well potential, the method is applicable to any one-dimensional (1D) potential problem [13, 63]. We conclude by discussing the extension to higher dimensions.

The variational Monte Carlo (VMC) technique is a powerful way to estimate the ground state of a quantum mechanical system. The basic idea is that one can use the variational principle to minimize the energy expectation value with respect to a set of parameters: $\{\alpha\}$

$$E(\alpha) = \frac{\int |\psi(x,\alpha)|^2 (H\psi)/\psi(x,\alpha))dx}{\int |\psi(x,\alpha)|^2 dx} \tag{5.78}$$

Following the Monte Carlo method for evaluating integrals, one interprets:

$$p(x)dx = \frac{|\psi(x,\alpha)|^2 dx}{\int |\psi(x,\alpha)|^2 dx} \tag{5.79}$$

as a probability distribution function. Typically, one assumes a functional form for the trial wave function, $\psi(x,\alpha)$, and the numerical advantage is that one can evaluate the energy integral by simply evaluating $\psi(x,\alpha)$. The method becomes variational when one then adjusts the parameters to optimize the trial wave function. Since the spectrum of H is bounded from below, the optimized trial wave function provides a best approximation to the true ground state of the system. However, since $p(x) = |\psi(x,\alpha)|^2$ is a positive definite function, this procedure fails if the system has nodes or if the position of the nodes is determined by the parameters. One can in principle obtain excitation energies by constraining the trial function to have a fixed set of nodes perhaps determined by symmetry.

Given that VMC is a robust technique for ground states, it would be highly desirable if the technique could be extended to facilitate the calculation of excited states. In this section, we present such an extension (albeit in one dimension) using SUSY QM. The underlying mathematical idea behind SUSY QM is that every Hamiltonian $H_1 = T + V_1$ has a partner Hamiltonian, $H_2 = T + V_2$ (T being the kinetic energy operator) in which the spectrum of H_1 and H_2 are identical for all states above the ground state of H_1. That is to say, the ground state of H_2 has the same energy as the first excited state of H_1 and so on. This hierarchy of related Hamiltonians and the algebra associated with the SUSY operators present a powerful formal approach to determine the energy spectra for a wide number of systems [5, 9, 26, 34, 39, 49, 55, 57, 72, 84, 89]. To date, little has been done exploiting SUSY QM as a way to develop new numerical techniques.

We shall first use the ideas of SUSY QM to develop a Monte Carlo-like scheme for computing the tunneling splittings in a symmetric double-well potential. While the model can be solved using other techniques, this provides a useful proof of principle for our approach. We find that the SUSY/VMC combination provides a useful and accurate way to obtain the tunneling splitting and excited state wave function for this system. While our current focus is on a 1D system, we conclude by commenting upon how the technique can be extended to multiparticle systems and to higher dimensions. In short, our results strongly suggest that this approach can be brought to bear on a more general class of problems involving multiple degrees of freedom. Surprisingly, the connection between the Monte Carlo technique and the SUSY hierarchy has not been exploited until recently [13, 63, 64].

5.5.1 *Supersymmetric quantum mechanics*

SUSY QM is obtained by factoring the Schrödinger equation into the form [29, 104, 105]:

$$H\psi = A^\dagger A\psi_o^{(1)} = 0 \tag{5.80}$$

using the operators:

$$A = \frac{\hbar}{\sqrt{2m}}\partial_x + W \tag{5.81}$$

$$A^\dagger = -\frac{\hbar}{\sqrt{2m}}\partial_x + W \tag{5.82}$$

Since we can impose $A\psi_o^{(1)} = 0$, we can immediately write that:

$$W(x) = -\frac{\hbar}{\sqrt{2m}}\partial_x \ln \psi_o \tag{5.83}$$

$W(x)$ is the *superpotential* that is related to the physical potential by a Riccati equation.

$$V(x) = W^2(x) - \frac{\hbar}{\sqrt{2m}}W'(x) \tag{5.84}$$

The SUSY factorization of the Schrödinger equation can always be applied in one dimension.

From this point on we label the original Hamiltonian operator and its associated potential, states, and energies as H_1, V_1, $\psi_n^{(1)}$ and

$E_n^{(1)}$. One can also define a partner Hamiltonian, $H_2 = AA^\dagger$, with a corresponding potential:

$$V_2 = W^2 + \frac{\hbar}{\sqrt{2m}} W'(x) \tag{5.85}$$

All of this seems rather circular and pointless until one recognizes that V_1 and its partner potential, V_2, give rise to a common set of energy eigenvalues. This principle result of SUSY can be seen by first considering an arbitrary stationary solution of H_1:

$$H_1 \psi_n^{((1)} = A^\dagger A \psi_n = E_n^{(1)} \psi_n^{(1)} \tag{5.86}$$

This implies that $(A\psi_n^{(1)})$ is an eigenstate of H_2 with energy $E_n^{(1)}$ since:

$$H_2(A\psi_n^{(1)}) = AA^\dagger A \psi_n^{(1)} = E_n^{(1)}(A\psi_n^{(1)}) \tag{5.87}$$

Likewise, the Schrödinger equation involving the partner potential $H_2\psi_n^{(2)} = E_n^{(2)}\psi_n^{(2)}$ implies that:

$$A^\dagger AA^\dagger \psi_n^{(2)} = H_1(A^\dagger \psi_n^{(2)}) = E_n^{(2)}(A^\dagger \psi_n^{(2)}) \tag{5.88}$$

This (along with $E_o^{(1)} = 0$) allows one to conclude that the eigenenergies and eigenfunctions of H_1 and H_2 are related in the following way: $E_{n+1}^{(1)} = E_n^{(2)}$,

$$\psi_n^{(2)} = \frac{1}{\sqrt{E_{n+1}^{(1)}}} A\psi_{n+1}^{(1)}, \text{ and } \psi_{n+1}^{(1)} = \frac{1}{\sqrt{E_n^{(2)}}} A^\dagger \psi_n^{(2)} \tag{5.89}$$

for $n > 0$.[a] Thus, the *ground state of H_2 has the same energy as the first excited state of* H_1. If this state $\psi_o^{(2)}$ is assumed to be nodeless; then $\psi_1^{(1)} \propto A^\dagger \psi_o^{(2)}$ will have a single node. We can repeat this analysis and show that H_2 is partnered with another Hamiltonian, H_3, whose ground state is isoenergetic with the first excited state of H_2 and thus isoenergetic with the second excited state of the original H_1. This hierarchy of partners persists until all of the bound states of H_1 are exhausted.

---

[a] Our notation from here on is that $\psi_n^{(m)}$ denotes the *n*th state associated with the *m*th partner Hamiltonian with a similar notation for related quantities such as energies and superpotentials.

5.5.2 *Implementation of SUSY QM in an adaptive Monte Carlo scheme*

Having defined the basic terms of SUSY QM, let us presume that one can determine an accurate approximation to the ground state density $\rho_o^{(1)}(x)$ of Hamiltonian H_1. One can then use this to determine the superpotential using the Riccati transform:

$$W_o^{(1)} = -\frac{1}{2}\frac{\hbar}{\sqrt{2m}}\frac{\partial \ln \rho_o^{(1)}}{\partial x} \tag{5.90}$$

and the partner potential:

$$V_2 = V_1 - \frac{\hbar^2}{2m}\frac{\partial^2 \ln \rho_o^{(1)}}{\partial x^2} \tag{5.91}$$

Certainly, our ability to compute the energy of the ground state of the partner potential V_2 depends on having first obtained an accurate estimate of the ground state density associated with the original V_1.

For this we turn to an adaptive VMC approach developed by Maddox and Bittner [82], as discussed earlier in this chapter. To recapitulate this approach, we assume we can write the trial density as a sum over N Gaussian approximate functions:

$$\rho_T(x) = \sum_n G_n(x, \mathrm{c}_n) \tag{5.92}$$

parameterized by their amplitude, center, and width.

$$G_n(x, \{\mathrm{c}_n\}) = c_{no}e^{-c_{n2}(x-c_{n3})^2} \tag{5.93}$$

This trial density then is used to compute the energy:

$$E[\rho_T] = \langle V_1 \rangle + \langle Q[\rho_T] \rangle \tag{5.94}$$

where $Q[\rho_T]$ is the Bohm quantum potential:

$$Q[\rho_T] = -\frac{\hbar^2}{2m}\frac{1}{\sqrt{\rho_T}}\frac{\partial^2}{\partial x^2}\sqrt{\rho_T} \tag{5.95}$$

The energy average is computed by sampling $\rho_T(x)$ over a set of trial points $\{x_i\}$ and then moving the trial points along the conjugate gradient of:

$$E(x) = V_1(x) + Q[\rho_T](x) \tag{5.96}$$

After each conjugate gradient step, a new set of $\mathrm{c_n}$ coefficients is determined according to an EM criteria such that the new trial density provides the best N-Gaussian approximation to the actual probability distribution function sampled by the new set of trial points. The procedure is repeated until $\delta\langle E\rangle = 0$. In doing so, we simultaneously minimize the energy and optimize the trial function. Since the ground state is assumed to be nodeless, we will not encounter the singularities and numerical instabilities associated with other Bohmian equations of motion-based approaches [12, 16, 52, 77, 82, 107].

5.5.3 *Test case: Tunneling in a double-well potential*

As a nontrivial test case, consider the tunneling of a particle between two minima of a symmetric double-well potential. One can estimate the tunneling splitting using semiclassical techniques by assuming that the ground and excited states are given by the approximate form:

$$\psi_\pm = \frac{1}{\sqrt{2}}(\phi_o(x) \pm \phi_o(-x)) \tag{5.97}$$

where ϕ_o is the lowest-energy state in the right-hand well in the limit the wells are infinitely far apart. From this, one can easily estimate the splitting as [67]:

$$\delta = 4\frac{\hbar^2}{m}\phi_o(0)\phi_o'(0) \tag{5.98}$$

If we assume the localized state (ϕ_o) to be Gaussian, then:

$$\psi_\pm \propto \frac{1}{\sqrt{2}}(e^{-\beta(x-x_o)^2} \pm e^{-\beta(x+x_o)^2}) \tag{5.99}$$

and we can write the superpotential as:

$$W = \sqrt{\frac{2}{m}}\hbar\beta\,(x - x_o\tanh(2xx_o\beta)) \tag{5.100}$$

From this, one can easily determine both the original potential and the partner potential as:

$$\begin{aligned} V_{1,2} &= W^2 \pm \frac{\hbar}{\sqrt{2m}}W' && (5.101) \\ &= \frac{\beta^2\hbar^2}{m}\,\big(2(x - x_o\tanh(2xx_o\beta))^2 \\ &\quad \pm (2x_o^2\operatorname{sech}^2(2xx_o\beta) - 1\big) && (5.102) \end{aligned}$$

While the V_1 potential has the characteristic double minima giving rise to a tunneling doublet, the SUSY partner potential V_2 has a central dimple, which in the limit of $x_o \to \infty$ becomes a δ-function, which produces an unpaired and nodeless ground state [29]. Using Eq. 5.88, one obtains $\psi_1^{(1)} = \psi_- \propto A^\dagger \psi_o^{(2)}$, which now has a single node at $x = 0$.

For a computational example, we take the double-well potential to be of the form:

$$V_1(x) = ax^4 + bx^2 + E_o \tag{5.103}$$

with $a = 438.9$ cm$^{-1}/(bohr^2)$, $b = 877.8$ cm$^{-1}/(bohr)^4$, and $E_o = -181.1$ cm^{-1}, which (for $m = m_H$) gives rise to exactly two states below the barrier separating the two minima with a tunneling splitting of 59.32 cm^{-1} as computed using a DVR approach [74]. For the calculations reported here, we used $n_p = 1000$ sample points and $N = 15$ Gaussians and in the expansion of $\rho_T(x)$ to converge the ground state. This converged the ground state to $1 : 10^{-8}$ in terms of the energy. This is certainly a bit of an overkill in the number of points and number of Gaussians since far fewer DVR points were required to achieve comparable accuracy (and a manifold of excited states). The numerical results, however, are encouraging since the accuracy of generic Monte Carlo evaluation would be $1/\sqrt{n_p} \approx 3\%$ in terms of the energy.[a] Plots of V_1 and the converged ground state are shown in Fig. 5.15.

The partner potential $V_2 = W^2 + \hbar W'/\sqrt{2m}$ can be constructed once we know the superpotential, $W(x)$. Here, we require an accurate evaluation of the ground state density and its first two log-derivatives. The advantage of our computational scheme is that one can evaluate these analytically for a given set of coefficients. In Fig. 5.15a we show the partner potential derived from the ground state density. Whereas the original V_1 potential exhibits the double-well structure with minima near $x_o = \pm 1$, the V_2 partner potential has a pronounced dip about $x = 0$. Consequently, its ground state should have a simple Gaussian-like form peaked about the origin.

---

[a] In our implementation, the sampling points are only used to evaluate the requisite integrals and they themselves are adjusted along a conjugate gradient rather than by resampling. One could in principle forego this step entirely and optimize the parameters describing the Gaussians directly.

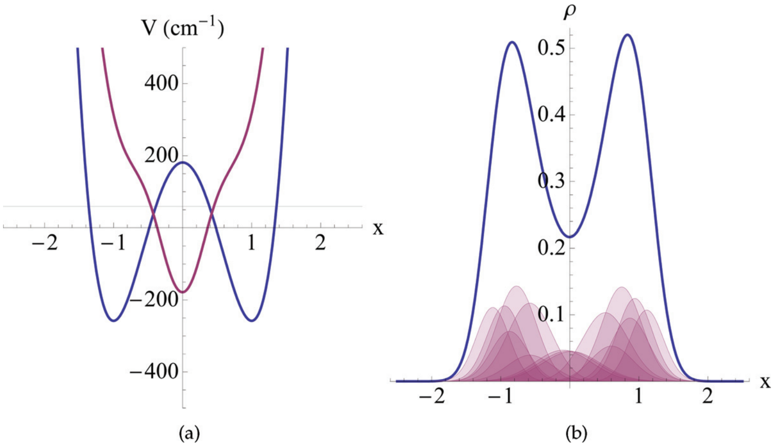

Figure 5.15. (a) Model double-well potential (blue) and partner potential (purple). The energies of the tunneling doublets are indicated by the horizontal lines at $V = 0$ cm^{-1} and $V = 59.32$ cm^{-1}, indicating the positions of the subbarrier tunneling doublet. (b) Final ground state density (blue) superimposed over the Gaussians used in its expansion (purple). Reprinted with permission from Ref. [13]. Copyright 2009 American Chemical Society.

Once we determined an accurate representation of the partner potential, it is now a trivial matter to reintroduce the partner potential into the optimization routines. The ground state converges easily and is shown in Fig. 5.16b, along with its Gaussians. After 1,000 CG steps, the converged energy is within 0.1% of the exact tunneling splitting for this model system. Again, this is an order of magnitude better than the $1/\sqrt{n_p}$ error associated with a simple Monte Carlo sampling. Furthermore, Fig. 5.16b shows $\psi_1^{(1)} \propto A^\dagger \psi_0^{(2)}$ computed using the converged $\rho_0^{(2)}$ density. As anticipated, it shows the proper symmetry and nodal position.

By symmetry, one expects the node to lie precisely at the origin. However, since we have not imposed any symmetry restriction or bias on our numerical method, the position of the node provides a sensitive test of the convergence of the trial density for $\rho_0^{(2)}$. In the example shown in Fig. 5.17, the location of the node oscillates about the origin and appears to converge exponentially with the number of CG steps. This is remarkably good considering that this is ultimately determined by the quality of the third and fourth derivatives of $\rho_o^{(1)}$

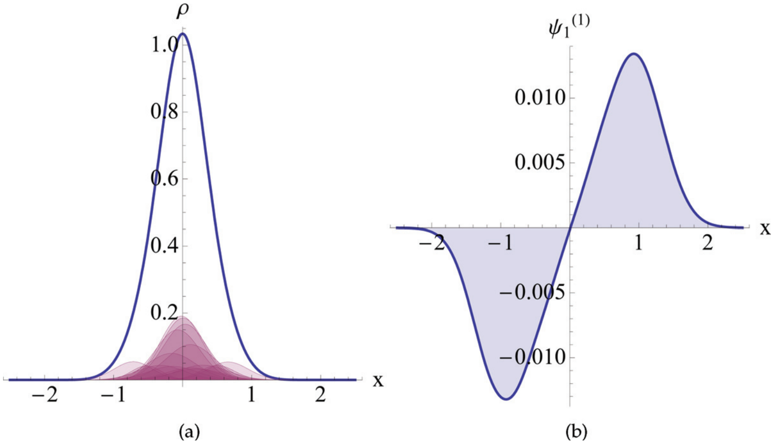

Figure 5.16. (a) Ground state density of the partner Hamiltonian H_2 (blue) superimposed over its individual Gaussian components. (b) Excited state $\psi_1^{(1)}$ derived from the ground state of the partner potential, $\psi_o^{(2)}$. Reprinted with permission from Ref. [13]. Copyright 2009 American Chemical Society.

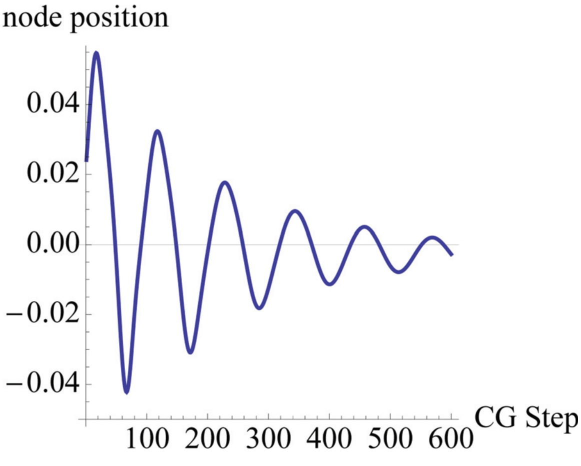

Figure 5.17. Location of excited state node for the last 600 CG steps. Reprinted with permission from Ref. [13]. Copyright 2009 American Chemical Society.

since these appear when computing the conjugate gradient of V_2. We have tested this approach on a number of other 1D bound-state problems with similar success.

5.5.4 *Extension to higher dimensions*

Having demonstrated that the SUSY approach can be used to compute excitation energies and wave functions starting from a Monte Carlo approach, the immediate next step is to extend this to arbitrarily higher dimensions. To move beyond 1D SUSY, Ioffe and coworkers have explored the use of higher-order charge operators [1–3, 25], and Kravchenko has explored the use of Clifford algebras [65]. Unfortunately, this is difficult to do in general. The reason being that the Riccati factorization of the 1D Schrödinger equation does not extend easily to higher dimensions. One remedy is to write the charge operators as vectors $\vec{A} = (+\vec{\partial} + \vec{W})$ and with $\vec{A}^{\dagger} = (-\vec{\partial} + \vec{W})^T$ as the adjoint charge operator. The original Schrödinger operator is then constructed as an inner-product:

$$H_1 = \vec{A}^{\dagger} \cdot \vec{A} \tag{5.104}$$

Working through the vector product produces the Schrödinger equation:

$$H_1 \phi = (-\nabla^2 + W^2 - (\vec{\nabla} \cdot \vec{W}))\phi = 0 \tag{5.105}$$

and a Riccati equation of the form:

$$U(x) = W^2 - \vec{\nabla} \cdot \vec{W} \tag{5.106}$$

For a 2D harmonic oscillator, we would obtain a vector superpotential of the form:

$$\vec{W} = -\frac{1}{\psi_0^{(1)}} \vec{\nabla} \psi_0^{(1)} = (x, y) = (W_x, W_y) \tag{5.107}$$

Let us look more closely at the $\vec{\nabla} \cdot \vec{W}$ part. If we use the form that $\vec{W} = -\vec{\nabla} \ln \psi$, then $-\vec{\nabla} \cdot \vec{\nabla} \ln \psi = -\nabla^2 \ln \psi$, which for the 2D oscillator results in $\vec{\nabla} \cdot \vec{W} = 2$. Thus:

$$W^2 - \vec{\nabla} \cdot \vec{W} = (x^2 + y^2) - 2 \tag{5.108}$$

which agrees with the original symmetric harmonic potential. Now, we write the scaled partner potential as:

$$U_2 = W^2 + \vec{\nabla} \cdot \vec{W} = (x^2 + y^2) + 2 \tag{5.109}$$

This is equivalent to the original potential shifted by a constant amount.

$$U_2 = U_1 + 4 \tag{5.110}$$

The ground state in this potential would be have the same energy as the states of the original potential with quantum numbers $n+m = 2$. Consequently, even with this naive factorization, one can in principle obtain excitation energies for higher-dimensional systems, but there is no assurance that one can reproduce the entire spectrum of states.

The problem lies in the fact that neither Hamiltonian H_2 nor its associated potential U_2 is given in its most general form by the expression implied by Eq. 5.105 and Eq. 5.109. Rather, the correct approach is to write the H_2 Hamiltonian as a *tensor* by taking the outer product of the charges $\overline{H}_2 = \vec{A}\vec{A}^\dagger$ rather than as a scalar $\vec{A} \cdot \vec{A}^\dagger$. At first this seems unwieldy and unlikely to lead anywhere since the wave function solutions of:

$$\overline{H}_2 \cdot \vec{\psi} = E\vec{\psi} \tag{5.111}$$

are now vectors rather than scalars. However, rather than adding an undue complexity to the problem, it actually simplifies matters considerably. As we demonstrate in a recent paper, this tensor factorization preserves the SUSY algebraic structure and produces excitation energies for any n-dimensional SUSY system [62].

5.5.4.1 Discussion

In brief, we have used the ideas of SUSY QM to obtain excitation energies and excited state wave functions within the context of a Monte Carlo scheme. This was accomplished without prespecifying the location of nodes or restriction to a specific symmetry. While it is clear that one could continue to determine the complete spectrum of H_1, the real challenge is to extend this technique to higher dimensions. Furthermore, the extension to multi-Fermion systems may be accomplished through the use of the Gaussian Monte Carlo method in which any quantum state can be expressed as a real probability distribution [4, 30].

5.6 Summary

In this chapter, we have explored an efficient strategy for determining the quantum density associated with a statistical ensemble of space-time trajectories. Given a statistical ensemble of probability elements, we can estimate the quantum force in terms of a set of Gaussian fitting parameters. Our methodology incorporates Bayesian probabilities and a mixture model approximation to calculate a parameterized estimate of Bohm's quantum force. The EM procedure used to fit the density is not sensitive to trajectory crossings because the error associated with an individual rogue trajectory is essentially washed out by the statistical ensemble. After a sufficient equilibration time the ensemble is representative of the ground state distribution and can be used to gather statistics on ground state properties such as the zero-point energy and other expectation values. Moreover, because the density fitting is formulated in terms of simple sums over data points, our method is easily extended to high dimensions and can be conveniently implemented on parallel computers.

We applied this approach to investigate the ground vibrational state energies at zero temperature and the low-temperature thermodynamics of mesoscopic rare gas clusters. Improvements in the algorithm allowed the calculation of the ground state structure at zero temperature, approaching the size necessary to simulate bulk systems. Our method compares favorably against path-integral Monte Carlo results on these systems and offers a systematic improvement over semiclassical treatments.

Finally, we present some of our most recent work in using the SUSY approach to compute quantum excited states using our adaptive approach. This work holds considerable promise in avoiding the node problem that has plagued both Monte Carlo and Bohmian trajectory approaches for years.

Most implementations of the Bohmian theory use trajectories as a way to gain deeper insight into a given problem or as a way to compute properties *given* a quantum density, we take more of *synthetic* approach to construct the quantum density from an ensemble of particles, which obey the Bohm quantum equations of motion. As discussed above, this presents a very difficult challenge, especially when extended to high-dimensional systems. The methods and results presented in this chapter represent the *first* successful implementations of a *synthetic* Bohmian approach that is robust, stable, and computationally efficient enough to study large numbers of atoms using realistic interatomic potentials. While we have not discussed it here, our approach can be used in conjunction with standard classical molecular dynamics algorithms to impart quantum-like behavior (such as tunneling) to specific atoms within the simulation.

Acknowledgements

The work at the University of Houston was funded in part by the National Science Foundation (CHE-1011894) and the Robert A. Welch Foundation (ERB: E-1334, DJK: E-0608). We also acknowledge fruitful discussions with Prof. R. E. Wyatt and Prof. Irene Burghardt concerning various aspects of the work presented in this chapter.

References

1. A. A. Andrianov, M. V. Ioffe, and V. P. Spiridonov, *Higher-Derivative Supersymmetry and the Witten Index*, Physics Letters A, **174**, 273 (1993).
2. A. A. Andrianov, M. V. Ioffe, and D. N. Nishnianidze, *Polynomial Supersymmetry and Dynamical Symmetries in Quantum Mechanics*, Theoretical and Mathematical Physics, **104**, no. 3, 1129–1140 (1995).
3. A. A. Andrianov, M. V. Ioffe, and D. N. Nishnianidze, *Polynomial SUSY in Quantum Mechanics and Second Derivative Darboux Transformations*, Physics Letters A, **201**, 103–110 (2002).
4. F. F. Assaad, P. Werner, P. Corboz, E. Gull, and M. Troyer, *Symmetry Projection Schemes for Gaussian Monte Carlo Methods*, Physical Review B, **72**, no. 22, 224518 (2005).
5. L. Balents and M. P. A. Fisher, *Delocalization Transition via Supersymmetry in One Dimension*, Physical Review B (Condensed Matter), **56**, no. 20, 12970–12991 (1997).

6. A. Banerjee and M. K. Harbola, *Hydrodynamic Approach to Time-Dependent Density Functional Theory; Response Properties of Metal Clusters*, Journal of Chemical Physics, **113**, no. 14, 5614–5623 (2000).
7. A. Banerjee and M. K. Harbola, *Calculation of van der Waals Coefficients in Hydrodynamic Approach to Time-Dependent Density Functional Theory*, Journal of Chemical Physics, **117**, no. 17, 7845–7851 (2002).
8. T. L. Beck and R. S. Berry, *The Interplay of Structure and Dynamics in the Melting of Small Clusters*, Journal of Chemical Physics, **88**, no. 6, 3910–3922 (1988).
9. V. Berezinsky and M. Kachelriess, *Monte Carlo Simulation for Jet Fragmentation in SUSY QCD*, Physical Review D (Particles and Fields), **63**, no. 3, 034007 (2001).
10. R. Stephen Berry, *Clusters: Tools for Studying Potential Surfaces and Their Connection to Molecular Dynamics*, Journal of Physical Chemistry, **98**, no. 28, 6910–6918 (1994).
11. E. R. Bittner, *Quantum Tunneling Dynamics Using Hydrodynamic Trajectories*, Journal of Chemical Physics, **112**, no. 22, 9703 (2000).
12. E. R. Bittner and R. E. Wyatt, *Integrating the Quantum Hamilton–Jacobi Equations by Wavefront Expansion and Phase Space Analysis*, Journal of Chemical Physics, **113**, no. 20, 8888 (2000).
13. E. R. Bittner, J. B. Maddox, and D. J. Kouri, *Supersymmetric Approach to Excited States*, Journal of Physical Chemistry A, **113**, no. 52, 15276–15280 (2009).
14. M. Bixon and J. Jortner, *Energetic and Thermodynamic Size Effects in Molecular Clusters*, Journal of Chemical Physics, **91**, no. 3, 1631–1642 (1989).
15. D. Bohm, *A Suggested Interpretation of the Quantum Theory in Terms of "Hidden" Variables. I*, Physical Review, **85**, 166 (1952).
16. D. Bohm, *A Suggested Interpretation of the Quantum Theory in Terms of "Hidden" Variables. II*, Physical Review, **85**, 180 (1952).
17. D. Bohm and B. Hiley, *The Undivided Universe: An Ontological Interpretation of Quantum Theory*, (Routlegde, 1993).
18. D. Bohm, B. J. Hiley, and P. N. Kaloyerou, *An Ontological Basis for the Quantum Theory*, Physics Reports, **144** (19878), 321.
19. D. F. R. Brown, M. N. Gibbs, and D. C. Clary, *Combining ab initio Computations, Neural Networks, and Diffusion Monte Carlo: An Efficient Method to Treat Weakly Bound Molecules*, Journal of Chemical Physics, **105**, no. 17, 7597 (1996).

20. J. C. Burant and J. C. Tully, *Nonadiabatic Dynamics via the Classical Limit Schrödinger Equation*, Journal of Chemical Physics, **112**, no. 14, 6097–6103 (2000).
21. I. Burghardt and L. S. Cederbaum, *Hydrodynamic Equation for Mixed Quantum States. I. General Formulation*, Journal of Chemical Physics, **115**, no. 22, 10303 (2001).
22. I. Burghardt and L. S. Cederbaum, *Hydrodynamic Equations for Mixed Quantum States. II. Coupled Electronic States*, Journal of Chemical Physics, **115**, no. 22, 10312 (2001).
23. W. Butine, *A Guide to the Literature on Learning Probabilistic Networks from Data*, IEEE Transactions on Knowledge Data Engineering, **8**, no. 2, 195 (1996).
24. F. Calvo, J. P. K. Doye, and D. J. Wales, *Quantum Partition Functions from Classical Distributions: Application to Rare-Gas Clusters*, Journal of Chemical Physics, **114**, no. 17, 7312–7329 (2001).
25. F. Cannata, M. V. Ioffe, and D. N. Nishnianidze, *New Methods for the Two-Dimensional Schrödinger Equation: SUSY-Separation of Variables and Shape Invariance*, Journal of Physics A: Mathematical and General, **35**, no. 6, 1389–1404 (2002).
26. F. Cannata, G. Junker, and J. Trost, *Solvable Potentials, Non-Linear Algebras, and Associated Coherent States*, Jakub Rembielinski and K. A. Smolinski (Eds.), vol. 453, pp. 209–218 (AIP, 1998).
27. C. M. Caves, C. A. Fuchs, and R. Schack, *Quantum Probabilities as Bayesian Probabilities*, Physical Review A, **65**, 022305 (2002).
28. D. M. Ceperley and E. L. Pollock, *Path-Integral Computation of the Low-Temperature Properties of Liquid* ^{4}*He*, Physical Review Letters, **56**, 351 (1986).
29. F. Cooper, A. Khare, and U. Sukhatme, *Supersymmetry and Quantum Mechanics*, Physics Reports, **251**, 267–385 (1995).
30. J. F. Corney and P. D. Drummond, *Gaussian Quantum Monte Carlo Methods for Fermions and Bosons*, Physical Review Letters, **93**, no. 26, 260401 (2004).
31. L. de Broglie, C. R. Academy of Sciences Paris, **183**, 24 (1926).
32. L. de Broglie, *Interference and Corpuscular Light*, Nature, **118**, 441–442 (1926).
33. L. de Broglie, C. R. Academy of Sciences Paris, **184**, 273 (1927).
34. R. de Lima Rodrigues, P. B. da Silva Filho, and A. N. Vaidya, *SUSY QM and Solitons from Two Coupled Scalar Fields in Two Dimensions*, Physical

Review D (Particles, Fields, Gravitation, and Cosmology), **58**, no. 12, 125023 (1998).

35. A. P. Dempster, N. M. Laird, and D. B. Rubin, *Maximum Likelihood from Incomplete Data via the EM Algorithm*, Journal of the Royal Statistical Society, Series B, **29** (1977).
36. S. W. Derrickson and E. R. Bittner, *Thermodynamics of Atomic Clusters Using Variational Quantum Hydrodynamics*, Journal of Physical Chemistry A, **111**, no. 41, 10345–10352 (2007).
37. S. W. Derrickson and E. R. Bittner, *A Self-Consistent Field Quantum Hydrodynamic Approach for Molecular Clusters*, Journal of Physical Chemistry A, **110**, no. 16, 5333–5341 (2006).
38. B. K. Dey, A. Askar, and H. Rabitz, *Multidimensional Wave Packet Dynamics within the Fluid Dynamical Formulations of the Schrödinger Equation*, Journal of Physical Chemistry, **109**, no. 20, 8770 (1998).
39. D. J. Fernández-C., and N. Fernández-García, *Higher-Order Supersymmetric Quantum Mechanics*, vol. 744, pp. 236–273 (AIP, 2004).
40. R. P. Feynman, *Statistical Mechanics: A Set of Lectures*, (Addison-Wesley, 1972).
41. R. P. Feynman and A. R. Hibbs, *Quantum Mechanics and Path Integrals*, (McGraw-Hill, 1965).
42. S. Garashchuk and V. A. Rassolov, *Semiclassical Dynamics Based on Quantum Trajectories*, Chemical Physics Letters, **364**, 562 (2002).
43. S. Garashchuk and V. A. Rassolov, *Semiclassical Dynamics with Quantum Trajectories: Formulation and Comparison with the Semiclassical Initial Value Representation Propagator*, Journal of Chemical Physics, **118**, no. 6, 2482–2490 (2003).
44. C. W. Gardiner, *Handbook of Stochastic Methods for Physics, Chemistry, and the Natural Sciences*, 2nd ed., Springer Series in Synergetics, vol. 13 (Springer-Verlag, New York, 1985).
45. N. Gershenfeld, *The Nature of Mathematical Modeling*, (Cambridge University Press, Cambridge, 1999).
46. E. Gindensperger, C. Meier, and J. A. Beswick, *Mixing Quantum and Classical Dynamics Using Bohmian Trajectories*, Journal of Chemical Physics, **113**, no. 21, 9369 (2000).
47. E. Gindensperger, C. Meier, and J. A. Beswick, *Quantum-Classical Dynamics Including Continuum States Using Quantum Trajectories*, Journal of Chemical Physics, **116** (2002).
48. E. Gindensperger, C. Meier, J. A. Beswick, and M. C. Heitz, *Quantum-Classical Description of Rotational Diffractive Scattering Using Bohmian*

Trajectories: Comparison with Full Quantum Wave Packet Results, Journal of Chemical Physics, **116**, no. 23, 10051 (2002).

49. M. Günther, J. Hellmig, G. Heusser, M. Hirsch, H. V. Klapdor-Kleingrothaus, B. Maier, H. Päs, F. Petry, Y. Ramachers, H. Strecker, M. Völlinger, A. Balysh, S. T. Belyaev, A. Demehin, A. Gurov, I. Kondratenko, D. Kotel'nikov, V. I. Lebedev, and A. Müller, *Heidelberg-Moscow $\beta\beta$ Experiment with ^{76}Ge: Full Setup with Five Detectors*, Physical Review D (Particles and Fields), **55**, no. 1, 54–67 (1997).
50. B. L. Hammond, W. A. Lester, and P. J. Reynolds, Monte Carlo methods in *ab initio* quantum chemistry, in *Lecture and Course Notes in Chemistry*, vol. 1 (World Scientific, River Edge, NJ, 1994).
51. E. J. Heller, *Frozen Gaussians: A Very Simple Semiclassical Approximation*, Journal of Chemical Physics, **75**, no. 6, 2923 (1981).
52. P. R. Holland, *The Quantum Theory of Motion: An Account of the de Broglie–Bohm Causal Interpretation of Quantum Mechanics*, (Cambridge University Press, 1993).
53. X. Hu, T. Ho, H. Rabitz, and A. Askar, *Solution of the Quantum Fluid Dynamical Equations with Radial Basis Function Interpolation*, Physical Review E, **61**, 5967 (2000).
54. K. E. Hughes and R. E. Wyatt, *Wavepacket Dynamics on Dynamically Adapting Grids: Application of the Equidistribution Principle*, Chemical Physics Letters, **366**, 336 (2002).
55. M. Humi, *Darboux Transformations for Schrödinger Equations in Two Variables*, Journal of Mathematical Physics, **46**, no. 8, 083515 (2005).
56. C. Huscroft, R. Gross, and M. Jarrell, *Maximum Entropy Method of Obtaining Thermodynamic Properties from Quantum Monte Carlo Simulations*, Physical Review B, **61**, no. 14, 9300 (2000).
57. A. Inomata and G. Junker, *Quasiclassical Path-Integral Approach to Supersymmetric Quantum Mechanics*, Physical Review A (Atomic, Molecular, and Optical Physics), **50**, no. 5, 3638–3649 (1994).
58. J. Jellinek, T. L. Beck, and R. S. Berry, *Solid-Liquid Phase Changes in Simulated Isoenergetic Ar_{13}*, Journal of Chemical Physics, **84**, no. 5, 2783–2794 (1986).
59. A. N. Korotkov, *Output Spectrum of a Detector Measuring Quantum Oscillations*, Physical Review B, **63**, 085312 (2001).
60. A. N. Korotkov, *Selective Quantum Evolution of a Qubit due to Continuous Measurement*, Physical Review B, **63**, 115403 (2001).
61. A. N. Korotkov, *Continuous Measurement of Entangled Qubits*, Physical Review A, **65**, 052304 (2002).

62. D. J. Kouri, K. Maji, T. Markovich, and E. R. Bittner, *New Generalization of Supersymmetric Quantum Mechanics to Arbitrary Dimensionality or Number of Distinguishable Particles*, Journal of Physical Chemistry A, **114**, no. 32, 8202–8216 (2010).
63. D. J. Kouri, T. Markovich, N. Maxwell, and E. R. Bittner, *Supersymmetric Quantum Mechanics, Excited State Energies and Wave Functions, and the Rayleigh–Ritz Variational Principle: A Proof of Principle Study*, Journal of Physical Chemistry A, **113**, no. 52, 15257–15264 (2009).
64. D. J. Kouri, T. Markovich, N. Maxwell, and B. G. Bodman, *The Heisenberg–Weyl Algebra on the Circle and a Related Quantum Mechanical Model for Hindered Rotation*, Journal of Physical Chemistry A, **113**, 7698–7705 (2009).
65. V. V. Kravchenko, *On the Reduction of the Multidimensional Stationary Schrödinger Equation to a First-Order Equation and Its Relation to the Pseudoanalytic Function Theory*, Journal of Physics A: Mathematical and General, **38**, 851 (2005).
66. P. Labastie and R. L. Whetten, *Statistical Thermodynamics of the Cluster Solid-Liquid Transition*, Physical Review Letters, **65**, no. 13, 1567–1570 (1990).
67. L. D. Landau and E. M. Lifshitz, Quantum mechanics (non-elativistic theory), in *Course of Theoretical Physics*, 3rd ed., vol. 3 (Pergammon, Oxford, 1974).
68. P. M. Lee, *Bayesian Statistics: An Introduction*, (Wiley, New York, 1997).
69. C. Leforestier, *A Comparison of Different Propagation Schemes for the Time Dependent Schrödinger Equation*, Journal of Computational Physics, **94**, 59 (1991).
70. J. C. Lemm and J. Uhlig, *Hartree–Fock Approximation for Inverse Many-Body Problems*, Physical Review Letters, **84**, no. 20, 4517 (2000).
71. J. C. Lemm, J. Uhlig, and A. Weiguny, *Bayesian Approach to Inverse Quantum Statistics*, Physical Review Letters, **84**, no. 10, 2068 (2000).
72. P. T. Leung, A. M. van den Brink, W. M. Suen, C. W. Wong, and K. Young, *SUSY Transformations for Quasinormal Modes of Open Systems*, Journal of Mathematical Physics, **42**, no. 10, 4802–4820 (2001).
73. J. C. Light, Discrete variable representations in quantum dynamics, in *Time-Dependent Quantum Molecular Dynamics*, J. Broeckhove and L. Lathouwers (Eds.), p. 185, (Plenum Press, New York, 1992).
74. J. C. Light, I. P. Hamilton, and J. V. Lill, *Generalized Discrete Variable Approximation in Quantum Mechanics*, Journal of Chemical Physics, **82**, no. 3, 1400–1409 (1985).

75. T. J. Liszka, C. A. M. Duarte, and W. W. Tworzydlo, *Computational Methods in Applied Mechanical Engineering*, **139**, 263 (1996).
76. D. M. Liveley, *Phase Separation in Freezing* ^{3}*He-Ne and* ^{4}*He-Ne Mixtures*, Journal of Physics C: Solid State Physics, **16**, 2889 (1983).
77. C. L. Lopreore and R. E. Wyatt, *Quantum Wavepacket Dynamics with Trajectories*, Physical Review Letters, **82**, 5190 (1999).
78. D. Lynden-Bell, *Negative Specific Heat in Astronomy, Physics and Chemistry*, Physica A: Statistical Mechanics and Its Applications, **263**, no. 1-4, 293–304, Proceedings of the 20th IUPAP International Conference on Statistical Physics (1999).
79. R. M. Lynden-Bell and D. J. Wales, *Free Energy Barriers to Melting in Atomic Clusters*, Journal of Chemical Physics, **101**, no. 2, 1460–1476 (1994).
80. J. B. Maddox and E. R. Bittner, *Quantum Relaxation Dynamics with Bohmian Trajectories*, Journal of Chemical Physics, **115**, no. 14, 6309 (2001).
81. J. B. Maddox and E. R. Bittner, *Quantum Dissipation in Unbounded Systems*, Physical Review E, **65**, 026143 (2002).
82. J. B. Maddox and E. R. Bittner, *Estimating Bohm's Quantum Force Using Bayesian Statistics*, Journal of Chemical Physics, **119**, no. 13, 6465–6474 (2003).
83. E. Madelung, Zeitschrift für Physik, **40**, 322 (1926).
84. J. Margueron and P. Chomaz, *Supersymmetry Transformation for Excitation Processes*, Physical Review C (Nuclear Physics), **71**, no. 2, 024318 (2005).
85. F. S. Mayor, A. Askar, and H. Rabitz, *Quantum Fluid Dynamics in the Lagrangian Representation and Applications to Photodissociation Problems*, Journal of Physical Chemistry, **111**, 2423 (1999).
86. G. J. McLachlan and K. E. Basford, *Mixture Models: Inference and Applications to Clustering*, (Marcel Dekker, New York, 1988).
87. G. J. McLachlan and K. E. Basford, *Mixture Models: Inference and Applications to Clustering*, (Dekker, New York, 1998).
88. N. David Mermin, *Thermal Properties of the Inhomogeneous Electron Gas*, Physical Review, **137**, no. 5A, A1441–A1443 (1965).
89. J. Niederle and A. G. Nikitin, *Extended Supersymmetries for the Schrödinger-Pauli Equation*, Journal of Mathematical Physics, **40**, no. 3, 1280–1293 (1999).

90. X. Oriols, J. J. García, F. Martín, J. Suñé, T. Gonzàlez, J. Mateos, and D. Pardo, *Bohm Trajectories for the Monte Carlo Simulation of Quantum-Based Devices*, Applied Physics Letters, **72**, 806 (1998).
91. X. Oriols, F. Martín, and J. Suñé, *High Frequency Components of Current Fluctuations in Semiconductor Tunneling Barriers*, Applied Physics Letters, **80**, no. 21, 4048–4050 (2002).
92. R. G. Parr and W. Yang, *Density Functional Theory of Atoms and Molecules*, (Clarendon Press, Oxford, England; Oxford University Press, New York, 1989).
93. C. Predescu, P. A. Frantsuzov, and V. A. Mandelshtam, *Thermodynamics and Equilibrium Structure of* Ne_{38} *Cluster: Quantum Mechanics versus Classical*, Journal of Chemical Physics, **122**, no. 15, 154305 (2005).
94. O. V. Prezhdo and C. Brooksby, *Quantum Backreaction through the Bohmian Particle*, Physical Review Letters, **86**, no. 15, 3215 (2001).
95. M. Schmidt, R. Kusche, T. Hippler, J. Donges, W. Kronmüller, B. von Issendorff, and H. Haberland, *Negative Heat Capacity for a Cluster of 147 Sodium Atoms*, Physical Review Letters, **86**, no. 7, 1191–1194 (2001).
96. M. Shapiro and R. Bersohn, *Vibrational Energy Distribution of the* CH_3 *Radical Phostodissociated from* CH_3I, Journal of Chemical Physics, **73**, no. 8, 3810 (1980).
97. J. Solca, A. J. Dyson, G. Steinebrunner, B. Kirchner, and H. Huber, *Melting Curves for Neon Calculated from Pure Theory*, Journal of Chemical Physics, **108**, no. 10, 4107–4111 (1998).
98. A. M. Steinberg, *How Much Time Does a Tunneling Particle Spend in the Barrier Region?*, Physical Review Letters, **74**, no. 13, 2405 (1995).
99. M. Toda, R. Kubo, and N. Saito, *Statistical Physics I: Equilibrium Statistical Mechanics*, (Springer, Berlin, 1992).
100. C. Trahan and R. E. Wyatt, *An Arbitrary Lagrangian–Eulerian Approach to Solving the Quantum Hydrodynamic Equations of Motion: Implementation with Smart Springs*, Journal of Chemical Physics, **118**, 4784 (2003).
101. C. F. von Weizsacker, Zeitschrift für Physik, **96**, 431 (1935).
102. Z. S. Wang, G. R. Darling, and S. Holloway, *Dissociation Dynamics from the de Broglie–Bohm Perspective*, Journal of Chemical Physics, **115**, no. 22, 10373 (2001).
103. H. M. Wiseman, S. Mancini, and J. Wang, *Bayesian Feedback versus Markovian Feedback in a Two-Level Atom*, Physical Review A, **66**, 013807 (2002).

104. E. Witten, *Dynamical Breaking of Supersymmetry*, Nuclear Physics B (Proceedings Supplements), **188**, 513 (1981).
105. E. Witten, *Supersymmetry and Morse Theory*, Journal of Differential Geometry, **17**, 661–692 (1982).
106. R. E. Wyatt, *Quantum Wave Packet Dynamics with Trajectories: Application to Reactive Scattering*, Journal of Chemical Physics, **111**, no. 10, 4406 (1999).
107. R. E. Wyatt, C. L. Lopreore, and G. Parlant, *Electronic Transitions with Quantum Trajectories*, Journal of Physical Chemistry, **114**, no. 12, 5113 (2001).
108. R. E. Wyatt and K. Na, *Electronic Transitions with Quantum Trajectories. II*, Journal of Physical Chemistry, **116**, 1228 (2002).
109. R. E. Wyatt and K. Na, *Quantum Trajectory Analysis of Multinode Subsystem-Bath Dynamics*, Physical Review E, **65**, 016702 (2002).
110. R. E. Wyatt, *Quantum Wavepacket Dynamics with Trajectories: Wave-function Synthesis along Quantum Paths*, Chemical Physics Letters, **313**, no. 1–2, 189–197 (1999).
111. T. Biben and D. Frenkel, *Density functional approach to helium at finite temperature*, Journal of Physics: Condensed Matter, **14**, 9077–9088, 2002.